Exclusion limits on the WIMP-nucleon cross section from the Cryogenic Dark Matter Search

D. Abrams,[8] D. S. Akerib,[2] M. S. Armel-Funkhouser,[9] L. Baudis,[8] D. A. Bauer,[10] A. Bolozdynya,[2] P. L. Brink,[8] R. Bunker,[10] B. Cabrera,[8] D. O. Caldwell,[10] J. P. Castle,[8] C. L. Chang,[8] R. M. Clarke,[8] M. B. Crisler,[3] R. Dixon,[3] D. Driscoll,[2] S. Eichblatt,[3] R. J. Gaitskell,[1] S. R. Golwala,[9] E. E. Haller,[4] J. Hellmig,[9] D. Holmgren,[3] M. E. Huber,[11] S. Kamat,[2] A. Lu,[10] V. Mandic,[9] J. M. Martinis,[5] P. Meunier,[9] S. W. Nam,[5] H. Nelson,[10] T. A. Perera,[2] M. C. Perillo Isaac,[9] W. Rau,[9] R. R. Ross,[4,9] T. Saab,[8] B. Sadoulet,[4,9] J. Sander,[10] R. W. Schnee,[2,*] T. Shutt,[6] A. Smith,[4] A. H. Sonnenschein,[10] A. L. Spadafora,[9] G. Wang,[2] S. Yellin,[10] and B. A. Young[7]

(CDMS Collaboration)

[1]*Department of Physics, Brown University, Providence, Rhode Island 02912*
[2]*Department of Physics, Case Western Reserve University, Cleveland, Ohio 44106*
[3]*Fermi National Accelerator Laboratory, Batavia, Illinois 60510*
[4]*Lawrence Berkeley National Laboratory, Berkeley, California 94720*
[5]*National Institute of Standards and Technology, Boulder, Colorado 80303*
[6]*Department of Physics, Princeton University, Princeton, New Jersey 08544*
[7]*Department of Physics, Santa Clara University, Santa Clara, California 95053*
[8]*Department of Physics, Stanford University, Stanford, California 94305*
[9]*Department of Physics, University of California, Berkeley, Berkeley, California 94720*
[10]*Department of Physics, University of California, Santa Barbara, Santa Barbara, California 93106*
[11]*Department of Physics, University of Colorado, Denver, Colorado 80217*

(Received 29 March 2002; published 20 December 2002)

The Cryogenic Dark Matter Search (CDMS) employs low-temperature Ge and Si detectors to search for weakly interacting massive particles (WIMPs) via their elastic-scattering interactions with nuclei while discriminating against interactions of background particles. For recoil energies above 10 keV, events due to background photons are rejected with $>99.9\%$ efficiency, and surface events are rejected with $>95\%$ efficiency. The estimate of the background due to neutrons is based primarily on the observation of multiple-scatter events that should all be neutrons. Data selection is determined primarily by examining calibration data and vetoed events. Resulting efficiencies should be accurate to $\sim 10\%$. Results of CDMS data from 1998 and 1999 with a relaxed fiducial-volume cut (resulting in 15.8 kg days exposure on Ge) are consistent with an earlier analysis with a more restrictive fiducial-volume cut. Twenty-three WIMP candidate events are observed, but these events are consistent with a background from neutrons in all ways tested. Resulting limits on the spin-independent WIMP-nucleon elastic-scattering cross section exclude unexplored parameter space for WIMPs with masses between 10–70 GeV/c^2. These limits border, but do not exclude, parameter space allowed by supersymmetry models and accelerator constraints. Results are compatible with some regions reported as allowed at 3σ by the annual-modulation measurement of the DAMA Collaboration. However, under the assumptions of standard WIMP interactions and a standard halo, the results are incompatible with the DAMA most likely value at $>99.9\%$ confidence level (C.L.), and are incompatible with the model-independent annual-modulation signal of DAMA at 99.99% C.L. in the asymptotic limit.

DOI: 10.1103/PhysRevD.66.122003 PACS number(s): 95.35.+d, 14.80.−j, 14.80.Ly

I. INTRODUCTION

This paper presents details of a new search for matter in the universe that is nonluminous, or ''dark.'' Extensive observational evidence indicates that this dark matter comprises a large fraction of the matter in the universe [1]. However, the nature and quantity of the dark matter in the universe remain unknown, providing a central problem for astronomy and cosmology [2,3]. Recent measurements of the cosmic microwave background radiation [4–6], as well as arguments based on big bang nucleosynthesis and the growth of structure in the universe [7], suggest that dark matter consists predominantly of nonbaryonic particles outside the standard model of particle physics. Supersymmetric particle physics models provide a natural candidate for dark matter: the lightest superpartner, usually taken to be a neutralino with typical mass about 100 GeV/c^2 [8–11]; experimental bounds from the CERN e^+e^- collider LEP give a lower limit of 46 GeV/c^2 [12].

More generically, one can consider a class of weakly interacting massive particles (WIMPs) [13], which were once in thermal equilibrium with the early universe, but were ''cold,'' i.e., moving nonrelativistically at the time of structure formation. Their density today is then determined roughly by their annihilation rate, with weak-scale interactions if the dark matter is mainly composed of WIMPs. WIMPs are expected to have collapsed into a roughly isothermal, spherical halo within which the visible portion of our galaxy resides, consistent with measurements of spiral galaxy rotation curves [14].

The best possibility for direct detection of WIMPS lies in

*Corresponding author. Email address: schnee@po.cwru.edu

elastic scattering from nuclei [15,16]. Calculations of the fundamental WIMP-quark cross sections require a model, usually the minimal supersymmetric standard model (MSSM) [8]. This interaction, summed over the quarks present in a nucleon, gives an effective WIMP-nucleon cross section. In the low momentum-transfer limit, the contributions of individual nucleons are summed coherently to yield a WIMP-nucleus cross section; these are typically smaller than 10^{-42} cm^2. The nuclear-recoil energy is typically a few keV [17], since WIMPs should have velocities typical for galactic objects.

Because of the extremely small WIMP scattering rate and the small energy of the recoiling nucleus, a direct-detection experiment must have a low energy threshold and very low backgrounds from radioactivity and cosmic rays (or be able to reject such backgrounds). The sensitivity of such an experiment improves linearly with detector mass, M, and exposure time, T, if there is no background. If there is a background of known size, the sensitivity can improve as $\propto\sqrt{MT}$.

The Cryogenic Dark Matter Search (CDMS) is an experiment designed to measure the nuclear recoils generated by galactic WIMPs using cryogenic Ge and Si detectors operating within a carefully shielded environment. CDMS detectors provide active rejection of backgrounds that would otherwise swamp any signal. Consequently, the assessment of detector performance, rejection efficiency, and known backgrounds constitutes a substantial component of our analysis effort.

This paper presents a new analysis of the data obtained by the CDMS Collaboration in its 1998 and 1999 experimental runs. The original analysis of these data and the associated exclusion limit on the WIMP-nucleon elastic-scattering cross section appeared in a Letter [18]. Significant changes introduced in this new analysis include a relaxed fiducial volume cut, resulting in a $\sim$40% larger exposure, as well as detailed treatment of possible systematic errors.

The organization of this paper is as follows. Section II describes the CDMS experimental apparatus, including the detectors, hardware, cryogenics, electronics, facilities, and data acquisition systems. Section III summarizes the methods by which the data are reduced and calibrated. Section IV presents the data obtained with the Ge detectors and details the application of cuts to the data. Because the measurements analyzed in this paper were made in a shallow facility, there is a significant unrejectable neutron background. Determination of this background is described in Sec. V. Section VI explains the procedure by which the limits on cross sections are calculated. Section VII contains the results of the new analysis including new limits on the WIMP-nucleon elastic-scattering cross section.

II. THE EXPERIMENT

The first stage of the Cryogenic Dark Matter Search (CDMS I) operates at the Stanford Underground Facility, a tunnel 10.6 m beneath the Stanford University campus. The experiment consists of a 2-m, nearly cubic, layered shield (with an active-scintillator muon veto) surrounding a cold volume which houses the Ge and Si detectors. The cold volume is connected via a horizontal stem to a dilution refrigerator and via a separate stem to a vacuum bulkhead where detector signals are brought out to front-end electronics. The amplified signals are coupled to a data acquisition system approximately 20 m away, where a trigger is formed and the signals are recorded. The Ge and Si detectors are cooled to sub-Kelvin temperatures so that the phonons produced by particle interactions are detectable above the ambient thermal phonon population. Simultaneous determination of the ionization energy and the phonon energy deposited in these Ge or Si crystals makes it possible to distinguish between a nuclear-recoil event produced by a WIMP (or a neutron) and an electron-recoil event due to the otherwise dominant background from radioactive decay products (mainly α particles, electrons, and photons). Such discrimination is possible because nuclear recoils dissipate a significantly smaller fraction of their energy into electron-hole pairs than do electron recoils [19].

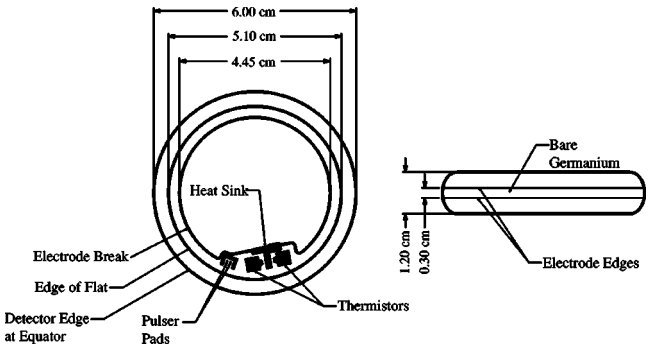

FIG. 1. A BLIP detector. The ionization-electrode breaks are indicated. The NTD thermistors are not shown in the side view; they are 0.26-cm high.

A. Detectors

The data discussed here were obtained with two types of detectors, Berkeley Large Ionization- and Phonon-mediated (BLIP) [19–21] and Z-sensitive Ionization- and Phonon-mediated (ZIP) detectors [22–26]. One early-design ZIP detector was operated in 1998, and four BLIP detectors were operated during a data run mostly in 1999.

Each BLIP detector consists of a cylindrical crystal of high-purity, undoped, p-type, single-crystal Ge with rounded edges, as shown schematically in Fig. 1. The BLIP substrates are 165 g in mass, 6 cm in diameter, and 1.2-cm thick. Phonon production is determined from the detector's calorimetric temperature change, as measured with two neutron-transmutation-doped (NTD) Ge thermistors (each approximately $3.1\times3.1\times2.6$ mm^3) eutectically bonded to the crystal [27]. Charge-collection electrodes on the top and bottom faces of each BLIP detector define the ionization drift field and provide electrical contact to the ionization bias circuits and amplifier [28]. For the 1999 data run, the four BLIP detectors (numbered 3–6 from top to bottom) were stacked 3 mm apart with no intervening material. This close packing helped shield the detectors from low-energy electron sources

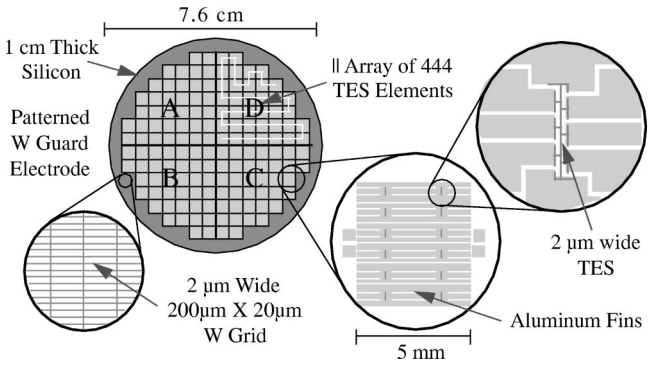

FIG. 2. A diagram of the phonon sensors for the 100-g Si ZIP detector run in 1998. The central item depicts the basic layout with each phonon sensor occupying a detector quadrant. Each sensor is divided into 37 units each 5 mm square (magnified to the right) which themselves contain 12 individual transition-edge-sensor (TES) elements (far right) connected in parallel. Aluminum quasiparticle-collector fins cover 82% of the top surface of the Si and also provide the ground electrode for the ionization measurement. On the far left is shown the W outer ionization electrode that is patterned (10% area coverage) to minimize athermal-phonon absorption.

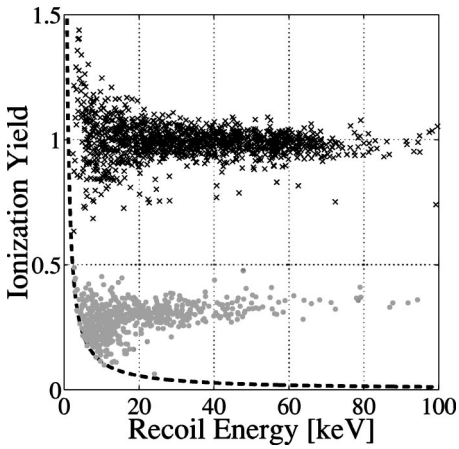

FIG. 3. Ionization yield Y versus recoil energy E_R for 1334 electron-recoil events due to photons from an external ^{60}Co source ($\times$'s) and for 616 nuclear-recoil events due to neutrons from a separate calibration with an external ^{252}Cf source (gray dots) for a Ge BLIP detector. These *in situ* external-source calibrations are described below in Sec. IV A. The dashed curve (at $E_Q = 1.1$ keV) indicates the ionization-search threshold (described below in Sec. IV B) for the neutron-calibration data.

on surrounding surfaces. The close-packing arrangement also increased the probability that a background event in one detector would multiple scatter into another detector. Division of the electrodes into an annular outer electrode and a disk-shaped inner electrode helped define an inner fiducial region that was further shielded from low-energy electron sources.

In ZIP detectors, athermal phonons are collected to determine both the phonon production and xy position of each event. The ZIP detector operated in 1998 is a high-purity, single-crystal cylinder of Si, 100 g in mass, 7.6 cm in diameter, and 1-cm thick. The detector has two concentric charge-collection electrodes. One side of the detector is patterned with an active aluminum and tungsten film that defines four independent phonon sensors (see Fig. 2). Around the perimeter of the phonon-sensor region is a passive tungsten grid, which provides 10% area coverage and is used in the ionization measurement.

The energy deposited in the detector by an interacting particle is called "recoil energy" E_R. If the particle interacts with an electron or electrons (e.g., by Compton scattering, K capture, etc.), the event is called an electron recoil; if the particle interacts with a nucleus (e.g., by WIMP-nucleus or neutron-nucleus elastic scattering), the event is a nuclear recoil. Most of the recoil energy is converted almost immediately into phonons, while the rest is dissipated via ionization losses in the creation of electron-hole pairs. By the time the calorimetric temperature rise is detected, the electron-hole pairs have recombined in the electrodes, releasing the energy initially dissipated in their creation. Thus, all of the recoil energy has been converted to phonons and is detected. In principle, a small fraction of the recoil energy can be lost to permanent crystal damage, to trapped charges, or to direct thermal conduction of high-energy, recombination phonons through a detector's electrodes. Comparisons of the collected phonon energy to kinematic energy measurements indicate at most a few percent of the recoil energy is lost [19,20,29].

Depending on the material and the type of recoil, between about one-sixteenth and one-third of the recoil energy is dissipated via ionization before subsequent conversion to phonons. On average, one electron-hole pair is produced for every $\epsilon \approx 3.0$ eV (3.8 eV) of energy from an electron recoil in Ge (in Si). The "ionization energy" E_Q is defined for convenience as the recoil energy inferred from the detected number of charge pairs N_Q by assuming that the event is an electron recoil with 100% charge-collection efficiency:

$$E_Q \equiv N_Q \times \epsilon. \tag{1}$$

Ionization energy is usually reported in units such as "keVee," or keV of the equivalent electron recoil. The ionization yield $Y \equiv E_Q/E_R$, so $Y \approx 1$ for electron recoils with complete charge collection.

Nuclear recoils produce fewer charge pairs, and hence less ionization energy E_Q, than electron recoils of the same recoil energy do. The ionization yield Y for nuclear-recoil events depends on both the material and the recoil energy, with $Y \sim 0.3$ ($Y \sim 0.25$) in Ge (in Si) for $E_R \gtrsim 20$ keV, as shown in Fig. 3 for Ge.

Energy is dissipated in the drifting of charges in the electric field, increasing phonon production by an amount equal to the work done by the electric field. These "Neganov-Luke" phonons contribute to the total observed phonon signal, yielding

$$E_P = E_R + eV_b N_Q = E_R + \frac{eV_b}{\epsilon} E_Q, \tag{2}$$

where V_b is the bias voltage across the detector [30,31]. Because the ionization measurement effectively weights the number of charge pairs by their drift distances (see Sec.

II A 1), this equation is valid even for events with incomplete charge collection (due, for example, to trapping or recombination in the wrong electrode). Since $E_Q = E_R$ for electron recoils with full charge collection, $E_P = [1 + (eV_b/\epsilon)]E_R$ for these events. Calibration of the detectors at several bias voltages using photon sources confirms that $\epsilon \approx 3$ eV (3.8 eV) in Ge (in Si). For electron recoils with full charge collection in Ge at 6 V bias (the bias voltage for most of the data described here), $E_P = 3E_R$. In practice, the recoil energy E_R of an event is inferred from measurements of the phonon and ionization energies:

$$E_R = E_P - \frac{eV_b}{\epsilon} E_Q. \quad (3)$$

1. The ionization measurement

Charge-collection electrodes deposited on the two faces of each disk-shaped detector are maintained at different voltages to supply an electric field, so that electrons drift toward one face and holes to the other. However, because the electrons and holes generated by an interaction are created ''hot'' and are not in local thermodynamic equilibrium with the crystal, some may diffuse before the drift field has a significant effect upon their motion. The charge cloud produced by a recoiling particle may also shield itself because the separating electron-hole pairs have dipole fields that counter the drift field. As a result, charges produced near a surface of the detector can diffuse against the applied electric field into the nearby electrode, causing a fraction of the event ionization to be ''lost.'' The surface region in which ionization is lost is termed the detector's ''dead layer'' [29].

In order to reduce the loss of ionization near detector surfaces, the BLIP detectors used in 1999 were made with hydrogenated, amorphous-silicon (α-Si) contacts [28]. Amorphous Si possesses a band gap $\epsilon_g = 1.2$ eV, almost twice as large as that of bulk Ge. As long as the bands of the bulk Ge and the deposited layer of α-Si are nearly centered on each other, the α-Si can block diffusion of charges of both polarities. See Fig. 4 for a schematic illustration of this effect. Data taken with test devices indicates that using α-Si contacts dramatically reduces the dead-layer problem [28,32].

The dead layer is a problem particularly for electrons incident on the surface of a detector, since electrons have a very small penetration depth. The 90% stopping length, or practical range, in Ge (in Si) is 0.5 μm (0.7 μm) at 10 keV, and is 10 μm (23 μm) at 60 keV. Although most low-energy electrons suffer incomplete ionization collection even with our α-Si electrodes, only a small fraction of the electrons produce an ionization yield indistinguishable from that characteristic of nuclear recoils.

As described below in Sec. IV, we have measured the efficiencies of our detectors for discriminating between nuclear recoils, bulk electron recoils, and surface electron recoils using conventional radioactive sources of neutrons, photons, and electrons. Above 10 keV, BLIP detectors reject bulk electron recoils with $>99.9\%$ efficiency and surface events with $>95\%$ efficiency. ZIP detectors provide further

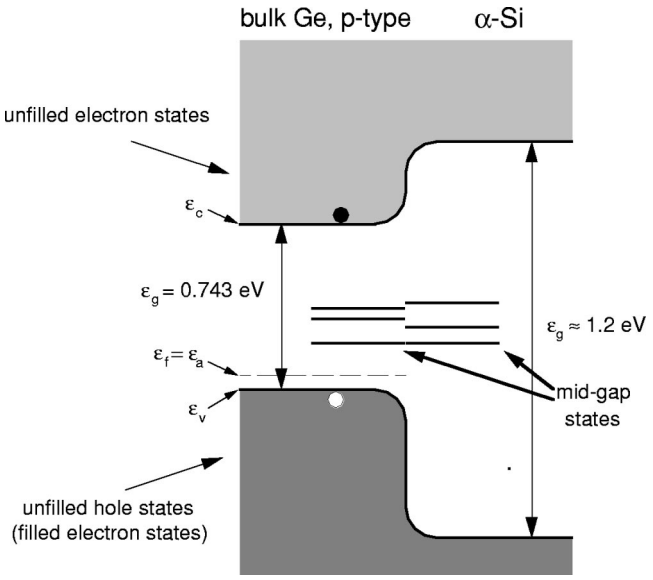

FIG. 4. Schematic illustration of bulk-Ge/α-Si interface, indicating qualitative misalignment suggested by data from test devices. Mid-gap states that may serve to define the alignment are schematically indicated.

surface-event rejection based on the differing phonon pulse shapes of bulk and surface events [25,26]. This phonon-based surface-event rejection alone is $>99.7\%$ efficient above 20 keV while retaining 40% of the nuclear-recoil events. Because the ZIP detector run in 1998 did not have α-Si electrodes, rejection of surface events in this detector was provided primarily by phonon pulse-shape analysis.

The ionization measurement depends on the drifting of charges to the detector's electrodes. The *p* type Ge has many more acceptor sites than donor sites, $N_A \gg N_D$, with number density $n_A - n_D \approx 6 \times 10^{10}$ cm^{-3}, and the dominant acceptor levels at $\epsilon_a \approx 12$ meV above the valence band. Because the detectors are cooled to ~ 20 mK, the number of free charges is Boltzmann suppressed by a factor $\exp(-\epsilon_a/kT) \sim e^{-5800}$ — i.e., there is no free charge. It is energetically favorable for the N_D electrons to fall onto acceptor sites rather than to bind to the N_D donor sites. If left alone, the resulting N_D ionized donor sites and N_D ionized acceptor sites would trap charges generated by events. Trapping is minimized, however, by neutralizing the ionized impurity sites once the detectors have been cooled, by exposing them to photons emitted by a light emitting diode (LED) while the detectors' electrodes are grounded [29]. Photons from the LED produce electron-hole pairs in the detector; the absence of a drift field allows these free charges to either recombine or be trapped on ionized impurities. When the detector is in the resulting neutralized state, charge-collection efficiency is 100%. The neutralized state degrades with time, presumably due to the liberation of trapped charges as drifting charges scatter off the trapping sites. Restoration of the neutralized state is accomplished by grounding the electrodes for a brief period; particle interactions (or additional flashes of light from an LED) create the necessary free charge to refill the traps. During the CDMS run in 1999, the BLIPs showed no signs of degraded ionization collection when used with a 50-min-biased/5-min-

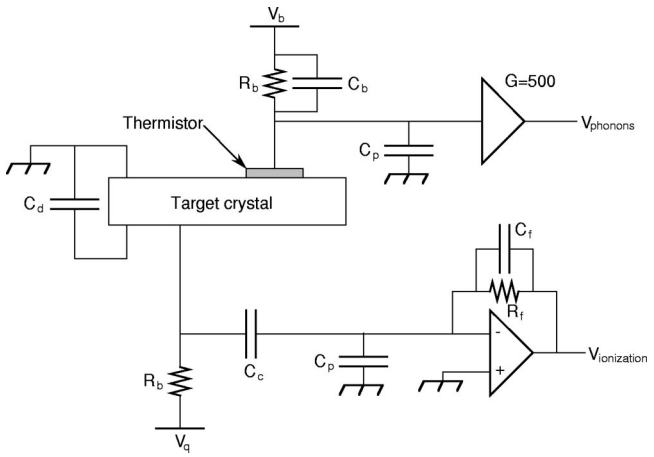

FIG. 5. Ionization-readout circuit used for both BLIPs and ZIPs, together with the BLIP phonon-readout circuit. The ionization amplifier connects to the biased side via a coupling capacitor with $C_c \approx 330$ pF. The detector capacitance $C_d \approx 40$ pF. The ionization-bias resistor $R_b = 40$ MΩ. The parasitic capacitance $C_p \approx 50$ pF is dominated by FET capacitance. This figure is taken from [33].

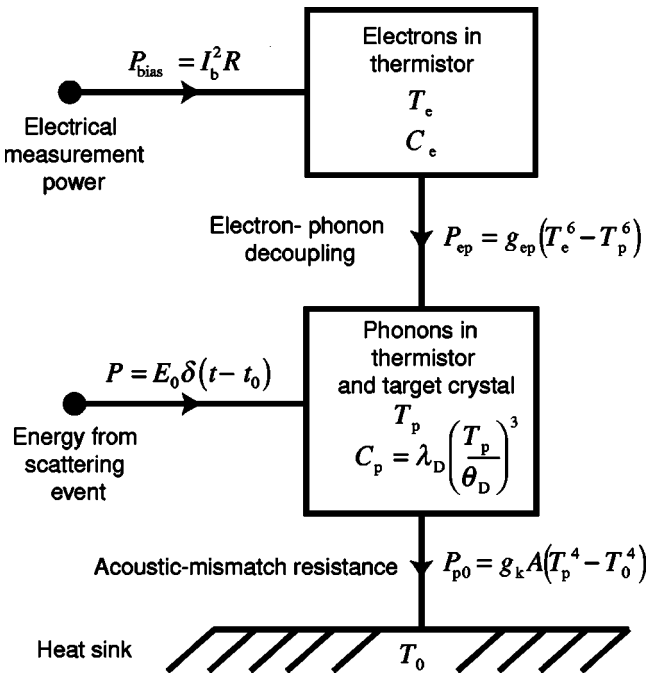

FIG. 6. BLIP thermal model. The top box is the electrons and the bottom the crystal or thermistor phonons. The heat sink is shown at the bottom. The power flows are described in the text. This figure is taken from [37].

grounded neutralization cycle. Slightly more conservative cycles were used in the 1998 run for the Si ZIP detector, with comparable results.

The readout circuit for the CDMS detectors is shown schematically in Fig. 5. Because the phonon circuit necessitates establishing a true ground on one side of the detector, the ionization amplifier is connected to the biased side through a coupling capacitor. The ionization amplifier operates as a current integrator; the signal observed is the voltage drop across the feedback capacitor, which collects a charge corresponding to the product of the number of electron-hole pairs created and the distance they drift across the detector. For complete charge collection, the total drift distance for a given pair is the the detector thickness, so the integrated charge simply gives the number of pairs created. When trapping occurs during drift, the integrated signal for a trapped charge is decreased to the fraction of the detector thickness across which it drifts before trapping. More details on the ionization- and phonon-readout electronics can be found in [25,34,35].

2. The BLIP phonon measurement

The BLIP detectors rely on the fact that the heat capacity of an insulating crystal drops as T^3 at low temperatures. Thus, very small depositions can cause large temperature rises. For a 165-g BLIP operated at 20 mK, a 10-keV deposition results in a measurable temperature rise of 2.4 μK.

The detector's coupling to the refrigerator is via a gold wirebond connecting the detector mount to a gold heat-sink pad deposited on the detector. The dominant thermal impedance is the area-dependent acoustic-mismatch resistance between the crystal substrate and the heat-sink pad. Thermal impedances within the heat-sink pad and the wirebond are negligible in comparison because these systems are metallic. Bias power dissipated in the thermistor heats the electron system in the thermistor and, to a lesser extent, the crystal to a few mK above the refrigerator temperature.

A simplified thermal model for BLIP detectors, including only one thermistor, is shown in Fig. 6. One system in this model includes the phonons in the crystal substrate and in the thermistors since the eutectic bond is transparent to phonons. The other system includes the thermistor's electrons, which can be taken to be separate from the phonon system because of the low-temperature phenomenon of electron-phonon decoupling. At these low temperatures, electron-phonon interaction rates are so low that the time needed for the electron and phonon systems of the thermistor to equilibrate with each other is significant compared to the internal thermalization times of the individual phonon and electron systems within the thermistor. Moreover, because a significant dc power is deposited into the electron system of a thermistor (in order to bias it), and the thermistor is heat-sunk via its phonons, a large steady-state temperature difference arises between electrons and phonons in the thermistor, as described in [36].

Schematically, the power flows are as follows. A thermistor-bias current I_b produces a measurable voltage $I_b R$. This dissipates power $I_b^2 R$ in the thermistor. (A current bias is needed to prevent thermal runaway because $dR/dT < 0$.) This power flows to the heat sink via the phonon system. An interaction in the crystal produces a δ-function energy deposition in the *phonon* system. The phonons heat up, warming the electrons via the electron-phonon coupling and yielding a measurable change in resistance. The energy flows out of the system via the connection to the heat sink. The couplings are chosen so the electron system senses the phonon-system temperature rise before the energy can leave the detector.

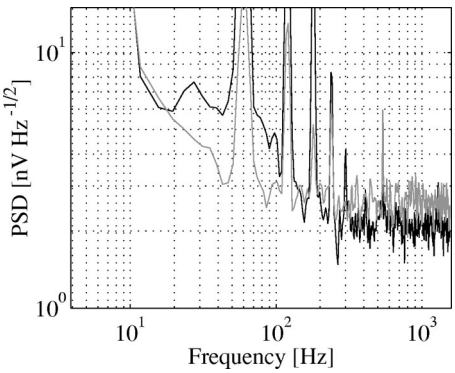

FIG. 7. Phonon-channel noise spectra without lockin, logarithmic scales. Dark line: phonon sensor 1. Light line: phonon sensor 2. The continuum noise, above about 100 Hz, is dominated by thermistor Johnson noise—the FET contributes ~ 1 nV/$\sqrt{\text{Hz}}$. The spectral lines are 60 Hz and harmonics. The significant increase in ''smooth'' noise and in 60 Hz and harmonics at low frequencies motivates the use of an ac modulation and demodulation technique: the fall and rise times of the phonon pulses correspond to ~ 3 Hz and ~ 30 Hz, so essentially all of the phonon signal is below 30 Hz.

Two thermistors are used to provide rejection of interactions in the thermistors. Use of two thermistors also decreases the phonon readout noise by $1/\sqrt{2}$. For crystal interactions and assuming the two thermistors are identical, the temperature-evolution solutions have the same form as a one-thermistor system: the two thermistors can be treated thermally and electrically as a single thermistor. For interactions within a single thermistor, the symmetry is broken and the results become more complicated, altering the signal shapes in the two thermistors.

The thermistor signal is a negative-going voltage pulse given by the product of the fixed bias current and the resistance decrease arising from an energy deposition. A low-noise voltage amplifier is used to measure this signal. The time constants are slow enough that a significant component of the signal lies at low frequencies. The rise and fall times of the BLIP phonon signals are ~ 5 ms and ~ 50 ms, corresponding to poles in the pulse frequency spectrum at ~ 30 Hz and ~ 3 Hz. Below 500 Hz, $1/f$ noise in the JFET, thermistor, or electrical connections, and spurious 60 Hz noise become significant; see Fig. 7. We have found it advantageous to use an ac modulation and demodulation technique for the BLIP phonon measurement. To take advantage of the very clean noise environment around 1 kHz, the dc current bias is replaced by a 1-kHz sine-wave bias [34,35,38].

3. The BLIP pulsers

In order to help calibrate each BLIP detector, a small resistive heater ($\sim 100\ \Omega$) on the detector surface is used to produce heat pulses. Additionally, pulser capacitors placed at the gates of the ionization-amplifier FETs allow δ-function current pulses to be sent to the ionization amplifiers [34]. These pulsers produce signals of fixed amplitude at known times, allowing measurement of the ionization and phonon energy resolutions as functions of energy (see Fig. 8). Every few hours during our normal data-acquisition process, a series of phonon-pulser events was taken. This data allows calibration of the effect of detector temperature on pulse height, allowing real-time corrections for small drifts in refrigerator temperature, as described in Sec. III C. For most of the run, ionization pulses were triggered by an asynchronous process, allowing independent measurement of the experiment live time and cut efficiencies.

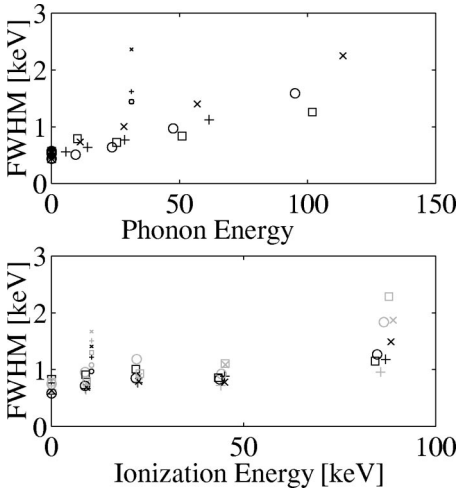

FIG. 8. Phonon energy resolutions and ionization electron-equivalent energy resolutions (full width, half maximum) as functions of energy for BLIP 3 (crosses), BLIP 4 ($\times$'s), BLIP 5 (circles), and BLIP 6 (squares), as measured using the pulsers, or the 10.4 keV (31.2 keV phonon energy) background line from gallium (small symbols). Resolutions of both the inner (black) and the outer (gray) ionization electrodes are shown. The apparent resolutions as determined by the widths of the 10.4 keV background line are likely worsened by the existence of another line at 9.65 keV. Phonon energy resolutions are worsened further by the effect of long-term drifts.

4. The ZIP phonon measurement

In contrast to the relatively slow, calorimetric measurement of phonon energy with the BLIP detectors, ZIP detectors rapidly detect athermal phonons before significant thermalization occurs, using quasiparticle-trap-assisted electrothermal-feedback transition-edge sensors [22]. These phonon sensors consist of photolithographically patterned, overlapping thin films of superconducting aluminum and tungsten, divided into 4 independent channels (see Fig. 2). Each channel contains a parallel array of 444 tungsten transition-edge sensors (TESs) each coupled to 6 aluminum phonon-collection pads.

Energy deposited in the bulk detector leads via anharmonic decay to generation primarily of high-frequency $\sim$THz (~ 4 meV), quasi-diffusive phonons [39]. These athermal phonons propagate to the detector surface, where most of them have enough energy ($>2\Delta_{\text{Al}} \approx 0.34$ meV) to be absorbed in 100-nm-thick, superconducting aluminum pads which cover 82% of the detector's surface [23,25]. Quasiparticles generated in the aluminum when the phonons break Cooper pairs diffuse in $\sim 10\ \mu$s through the alumi-

num to the detector's tungsten TES, where they become trapped. Through electron-electron interactions, these quasiparticles rapidly lose their potential energy by heating the conduction electrons in the tungsten, which has no gap since the tungsten film is biased in the middle of its superconducting-to-normal transition. The net result is that a few percent of the energy in athermal phonons from an event in the detector substrate is measured in the tungsten TES. For the ZIP detector run in 1998, this collection efficiency was $\sim 2\%$.

The TESs are voltage biased, and the current through them is monitored by a high-bandwidth HYPRES superconducting quantum interference device (SQUID) array [40,41]. The phonons released in the tungsten raise the temperature of the film, increasing its resistance and reducing the current. To ensure operation in the extreme feedback limit, the substrate is kept much colder ($T < 50$ mK) than the transition temperature of the tungsten sensor ($T_c \sim 80$ mK). The tungsten is maintained stably within the transition by electrothermal feedback based on Joule self-heating: if the sensor were hotter, the resistance would increase, decreasing the current and the Joule heating; an analogous argument applies if the sensor were cooler. The interaction energy deposited in the tungsten as phonons is entirely removed by the reduction in Joule heating caused by the current drop. Therefore, in the limit of very sharp transitions, the energy absorbed by the tungsten is just the integral of the current drop times the bias voltage:

$$E = V_b \int \delta I dt. \tag{4}$$

The tungsten sensors are intrinsically very fast, with pulse rise times electronics bandwidth limited (at ~ 100 ns), and fall times governed by the electrothermal feedback time ($20-40$ μs). The actual pulse shapes measured from ZIP phonon sensors are dependent on both the phonon propagation in the detector substrate, and the quasiparticle diffusion in the Al collection fins. The pulses typically have rise times in the range $5-15$ μs, and fall times ~ 100 μs, dominated by the phonon collection. Comparison of phonon-pulse arrival times in the four independent channels allows localization in the xy plane of a ZIP detector. In addition, energy deposited near detector surfaces apparently gives rise to slightly lower-frequency phonons, which undergo less scattering and hence travel ballistically [26]. The shorter rise times of the resulting phonon pulses allow rejection of such surface events.

B. Cryogenics

The detectors are located inside a large cold volume [42,43]. The nested cans of the cryostat, each of which corresponds to a thermal stage in our modified Oxford Instruments S-400 dilution refrigerator, serve as both thermal radiation shields and heat sinks for detector wiring and support structures. The cryostat is connected to the dilution refrigerator via a copper coldfinger and a set of coaxial copper tubes. Each tube connects one can to the corresponding thermal stage in the refrigerator, with the copper coldfinger connecting the innermost can directly to the mixing chamber. The nominal temperatures of the cryostat cans (and refrigerator thermal stages) are 10 mK, 50 mK, 600 mK, 4 K, 77 K, and 300 K. The cryostat itself contains no cryogenic liquid; all cooling power is generated in the refrigerator, and the cryostat is cooled via conduction. The innermost can is 30 cm in diameter and 30 cm high, providing approximately 21 liters of experimental space at ~ 20 mK base temperature. Access to this space is obtained by removing the can lids.

A cryogenic detector readout package addresses the unusual combination of requirements in CDMS—low noise, low background, high channel count, and low temperature [35]. The anchor for the system is a multi-temperature-stage modular coaxial wiring package, or ''tower.'' Directly below the tower are mounted up to six detector holders with modular coaxial wiring assemblies. Mounted on top of the tower are cold electronics cards that carry either four field-effect transistors (FETs) (for a BLIP detector), or four dc SQUID arrays and two FETs (for a ZIP detector). Because of the susceptibility to microphonic pickup for the gate wires of the FET, a vacuum coaxial geometry is used in which the wires are tensioned and attached to a printed circuit board at the ends of covered copper channels. The absence of a dielectric near the gate wires minimizes the presence of static charge, thereby reducing microphonic pickup. The printed circuit boards also serve to heatsink the wires to the various temperature stages. The electrical connections from the FET/SQUID cards at 4 K to the room-temperature vacuum bulkhead feedthroughs are made through a 3-m-long shielded copper-kapton flex circuit, or ''stripline.'' The tower and detector packaging is constructed so that infrared radiation from room temperature and the 130 K FETs is efficiently blocked and absorbed at each layer. Except for the warm end of the stripline, which is outside the radioactive shielding, all of the components of the towers, stripline, electronics cards and detector packages are made from materials that have been prescreened for U/Th isotopes, with the goal of having < 0.1 ppb of the mass of the material surrounding the detector package, or approximately < 1 μBq/g. One such material is a custom-made low-activity solder [44].

C. The Stanford Underground Facility

Due to the cryogenic technology and continuing development of our Ge and Si detectors, the initial dark matter search has been conducted at a local site. The Stanford Underground Facility (SUF) is a tunnel 10.6 m below ground level in the Hansen Experimental Physics Laboratory on the Stanford University campus. The tunnel housing the experiment is a clean area supplied with cooled, filtered air from the surface to suppress radon. The earth above SUF absorbs the hadronic component of cosmic-ray showers which would otherwise produce a large background rate and activate materials near the detectors. The overburden also reduces the muon flux by a factor of 5; the muon flux measurements indicate that the overburden is equivalent to ~ 16 m of water. A substantial vertical muon flux ($29\ \mathrm{m}^{-2}\ \mathrm{s}^{-1}\ \mathrm{sr}^{-1}$) is still present in the SUF tunnel due to the relatively shallow depth. The muon-induced neutron flux, and the ambient photons

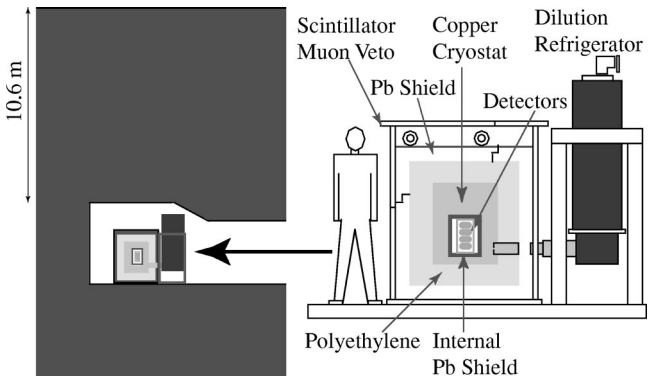

FIG. 9. Layout of the CDMS I shielding at the Stanford Underground Facility.

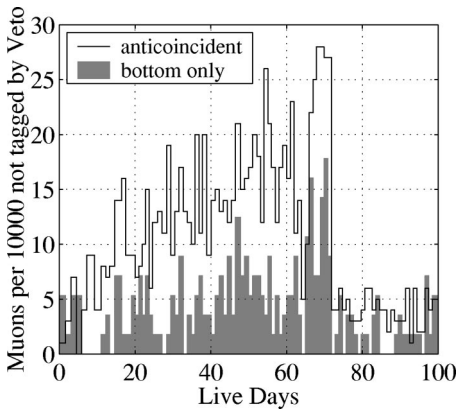

FIG. 10. Veto inefficiency for detector-tagged muons during the 1999 Ge data run described in Sec. IV. The dark, unfilled histogram indicates the number of detector-through-going muons anticoincident with the muon veto per 10 000 detector-through-going muons detected. The gray, shaded histogram shows the fraction of muons passing through both a detector and the bottom layer of the veto that were not tagged by one of the other sides of the veto. The performance of the veto slowly degraded over the course of the run. It was improved briefly on June 20 (live day 64). It was improved more permanently on July 30 (live day 72). See Fig. 14 for the dates corresponding to the integral live days into the run.

and neutrons from radioactivity in the tunnel walls, dictate that a passive shield and an active veto surround the detectors.

D. Shielding and muon veto

The goal of shielding is to minimize the rate of interactions arising from external particle sources that can mimic nuclear recoils in the cryogenic detectors. These external sources include photons and neutrons from radioactivity in the surrounding environment, photons and neutrons produced by cosmic-ray muons, and electrons from radioactivity on surfaces. The external sources are primarily from the ^{238}U and ^{232}Th decay chains, with photon energies up to 2.6 MeV, and from ^{40}K, which emits a 1.46 MeV photon. Passive shielding consisting of lead, polyethylene, and copper reduces the flux from radioactive contamination, while active shielding efficiently vetoes the flux produced by muons from cosmic rays.

The concentric shields around the WIMP detectors at SUF are shown schematically in Fig. 9. Outermost is the active veto [37], fashioned of a NE-110 plastic scintillator with waveshifter bars coupled to 2″ RCA 8575 photomultiplier tubes (PMTs). Each scintillator is coupled to 1–4 PMTs, depending on its size and shape. The PMT signals are summed together for each scintillator, then presented to LeCroy NIM discriminators. The discriminator thresholds are set to be sensitive to (minimum-ionizing) cosmic-ray muons, which deposit about 8 MeV in the 4.1-cm-thick scintillator, and insensitive to the vast majority of photons from radioactivity, whose spectrum ends at 2.6 MeV. To reject events in the detectors that occur close in time with the passage of a muon, we record the times of all veto hits above threshold in a ± 10 ms window about each detector trigger and use a ~ 25 μs window to establish correlations. The total veto-trigger rate during normal operation is approximately 6 kHz, leading to $\sim 15\%$ dead time due to accidental correlations. To monitor possible changes in veto performance, analog-to-digital converters read out the pulse heights from all six sides of the veto for each event.

A thorough mapping of the veto with an x-ray source documented a few areas of relatively poor light collection in late 1998, just before the start of the 1999 Ge data run described in Sec. IV. To compensate, high voltages and thresholds for all veto counters were tuned to ensure that muons passing through these areas would not be missed (at the expense of reduced live time due to a higher rate of vetoing by environmental photons passing through the areas of the counter with better light collection). The efficiency of the veto for detecting muons can be measured using muons identified by their large energy depositions in the Ge detectors. The average measured efficiency of this veto for muons during the 1999 Ge data run described in Sec. IV was 99.9%, with time variation shown in Fig. 10. The rejection inefficiency for cosmic-induced neutrons generated in material surrounded by the veto should be $\sim 3\times$ worse ($\sim 0.3\%$); this rejection efficiency is sufficient to reduce the background from these neutrons to a level comparable to the background from neutrons produced outside the veto. The measured efficiency of the veto for muons during the 1998 data run is even higher, 99.995%.

The veto surrounds a lead shield of 15 cm thickness, which attenuates the external photon flux by a factor of 1000. The inner 5 cm of this lead shell is made from Glover lead, which has substantially less of the long-lived (22-year half-life) ^{210}Pb isotope which is present at some measurable level in all sources of recently manufactured lead [45]. Decays of ^{210}Pb yield a bremsstrahlung spectrum (from ^{210}Bi with a 1.16 MeV end point), which results in background photons that interact in the detectors. Inside the lead, a 25-cm thickness of polyethylene surrounds the cryostat. The polyethylene moderates and attenuates neutrons from the material surrounding the tunnel and from the interaction of cosmic-ray muons with the lead shield. Previous studies at this depth indicate that thicker polyethylene would increase the neutron flux at the detectors due to neutron production in the polyethylene itself. The cryostat and detector-wiring assembly constitute an average thickness of about 3 cm of copper. The

most important contribution of the veto is to reject events from neutrons produced by cosmic-ray muons entering this copper. Samples of all construction materials were screened to ensure low radioactive contamination. A 1-cm-thick ''internal'' shield made of ancient Pb, which has very little ^{210}Pb, immediately surrounds the detectors in order to further reduce the photon background [46]. The layers of the shield outside the cryostat can be partially lifted and rolled away for easy access to the detector volume. None of the shielding is hermetic because copper tubes providing cooling or electrical connections must penetrate the shields; however, shielding inside these copper tubes helps reduce the external photon flux.

E. Expected backgrounds

The shielding was designed in conjunction with Monte Carlo simulations and measurements of particle fluxes at SUF [33,47]. The measured event rate between 10–100 keV in Ge detectors due to photons is roughly 60 $\mathrm{keV}^{-1}\,\mathrm{kg}^{-1}\,\mathrm{d}^{-1}$ overall and 2 $\mathrm{keV}^{-1}\,\mathrm{kg}^{-1}\,\mathrm{d}^{-1}$ anticoincident with the veto. These anticoincident photons are presumably due to residual radioactivity in and around the inner shielding and detector package. Detector discrimination of 99.9% should reduce the photon background to $\approx 5 \times 10^{-4}$ events $\mathrm{keV}^{-1}\,\mathrm{kg}^{-1}\,\mathrm{d}^{-1}$, negligible compared to other expected backgrounds. The non-muon-induced low-energy-electron background is more difficult to predict, as it depends critically on the level of radioactive contamination on parts immediately next to the detectors. This background is also potentially more troubling because of the CDMS detectors' ionization dead layer. Discussion of the measured low-energy-electron background is described in Sec. IV.

The rate of neutrons from natural radioactivity of materials inside the shield is negligible because of the careful choice of construction materials. Neutrons from natural radioactivity in the tunnel walls and outer lead can also be ignored; because their spectrum is softer than that of neutrons produced by muons, they are well moderated by the polyethylene. Neutrons with energies capable of producing keV nuclear recoils in the detectors are produced by muons interacting inside or outside the veto (''internal'' or ''external'' neutrons, respectively). The dominant, low-energy ($<$50 MeV) component of these neutrons is moderated well by the polyethylene [47]. Essentially all remaining internal neutrons are tagged as muon-coincident by the scintillator veto. However, relatively rare, high-energy external neutrons may ''punch through'' the polyethylene and yield secondary neutrons that produce keV nuclear recoils. A large fraction of the events induced by high-energy external neutrons are vetoed: $\sim$40% due to neutron-scintillator interactions, and an unknown fraction due to hadronic showers associated with the primary muon. This unknown fraction, combined with a factor of 4 uncertainty in their production rate, makes it difficult to accurately predict the absolute flux of unvetoed external neutrons.

Two methods are used to *measure* this flux of unvetoed external neutrons. The first method involves comparing the rate of nuclear-recoil events in the Ge detectors with the rate in the Si detector, since Ge is more sensitive to WIMPS and Si is more sensitive to neutrons. The second method is to count the number of events consisting of nuclear recoils in two or more detectors. Since WIMPs interact too weakly to multiple scatter, these events must be due to neutrons, thereby providing a clean measurement of the neutron background. Predictions from Monte Carlo simulations of the expected ratio of single-detector scatters to multiple-detector scatters are then used to determine the expected rate of neutron single-scatter events. Neutron backgrounds are simulated using the MICAP [48] and FLUKA [49] extensions to the GEANT [50] particle-physics simulation package. The MICAP and FLUKA packages track neutrons above and below 20 MeV, respectively. For this work, no attempt is made to simulate the production of the neutrons. Instead, production rates and spectra from [51] are used, and only the propagation of the neutrons and their interactions in the detectors are simulated. These simulations will be discussed further in Sec. V.

F. Data acquisition

The purpose of the data acquisition system for CDMS (shown as the block diagram in Fig. 11) is to generate an experimental trigger and faithfully record all detector and veto activity within a specified time interval about that trigger. Detector signals from the front-end electronics are received, conditioned, and anti-alias-filtered in custom 9U electronics boards. These boards also contain discriminators which provide low-threshold ionization-trigger and phonon-trigger signals, as well as high-threshold trigger signals for vetoing high-energy events during calibrations. The trigger signals are combined in a separate 9U board which generates a global trigger signal to inform the data acquisition computer that an event has occurred. The individual trigger signals are also stored in a history buffer (VXI Technology 1602, clocked at 1 MHz), which preserves a triggering history for up to 10 ms before and after each global trigger. Trigger thresholds and logic are configured via a backplane digital bus that is interfaced to GPIB.

The filtered detector pulses are routed to VME waveform digitizers (Omnibyte Comet and Joerger VTR1012) situated in a VXI mainframe, which provides better ambient noise rejection than VME crates. These 12-bit, 5–10 MHz digitizers record the entire waveform, or trace, for each detector channel, including the pre-trigger baselines. This information is crucial for extracting the best signal-to-noise ratio from the detectors, and for rejecting artifacts such as pulse pile-up, at a cost of large event sizes (typically 50–100 kB).

The muon-veto PMT signals are processed by NIM discriminators and logic, then recorded in a VXI history buffer (VXI Technology 1602) which is clocked at 1 MHz. A buffer extending on average from 15 ms before trigger to 5 ms after trigger is read out on every trigger, allowing correlations with cosmic-ray muons to be made strictly in software.

Monitoring information is provided by GPIB and CAMAC instruments. The dilution refrigerator and cryostat temperatures and pressures are sampled every 30 min, while detector temperatures, trigger or veto rates, and veto high

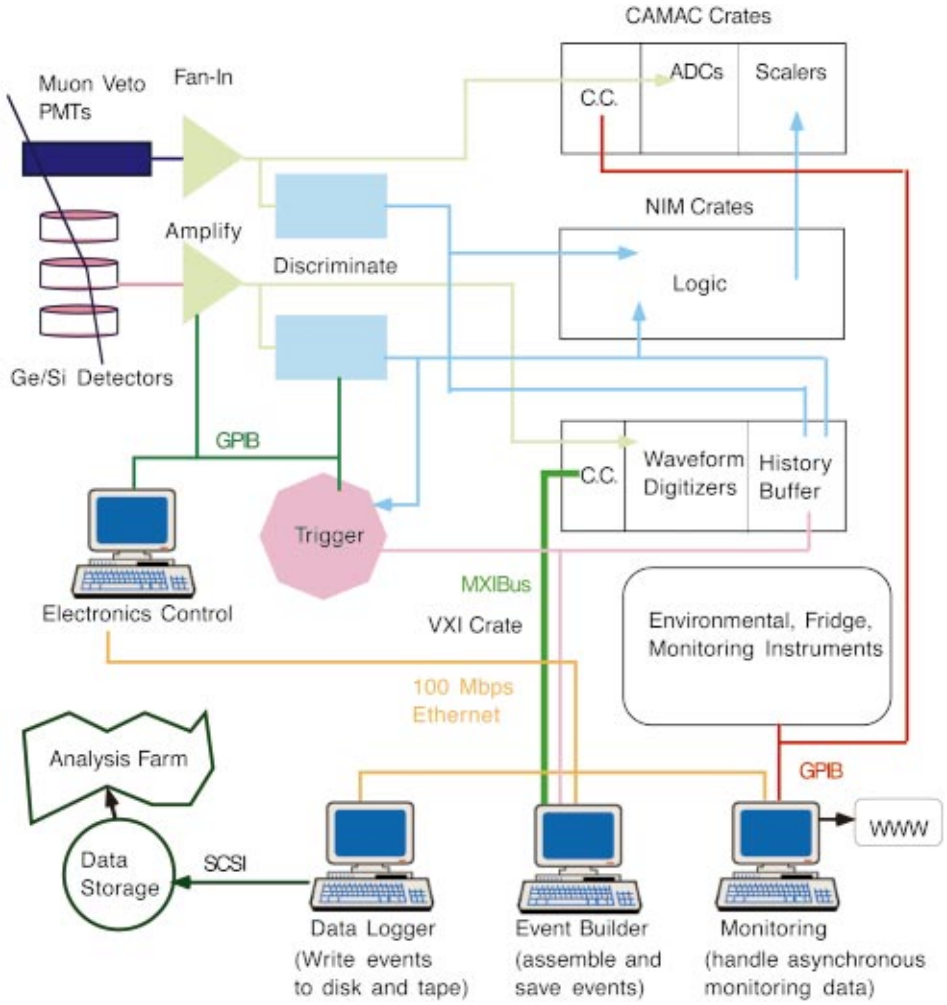

FIG. 11. (Color) Block diagram of the CDMS data acquisition system.

voltages are measured once a minute. This information is constantly on display at SUF and is remotely accessible from any World Wide Web browser. Email and phone alarms warn of serious problems.

The online data acquisition software is written in LABVIEW [52] and runs on a cluster of Power Macintoshes. The system is modular, in that the main event-builder program runs on one computer which communicates over a high-speed link to the VXI crate, while all front-end control and environmental monitoring runs on separate computers. A VME I/O module (HP 1330B) synchronizes the software to the trigger hardware and provides the path for a random (software) trigger to be recognized by the hardware. The online acquisition system is capable of running with better than 85% live time for up to six detectors at the typical total low-background trigger rate of ~ 0.4 Hz. Data are written over the local Fast Ethernet (100 Mbps) network to fast SCSI disks, where it is promptly analyzed via a MATLAB/C analysis system running on Unix/Linux workstations. Both raw data and summary information are written to DLT tapes.

III. Ge BLIP DATA REDUCTION

Automated analysis reduces the detector pulses (see Fig. 12) to quantities describing the energies, times, and quality of various fits performed. First, it is necessary to determine

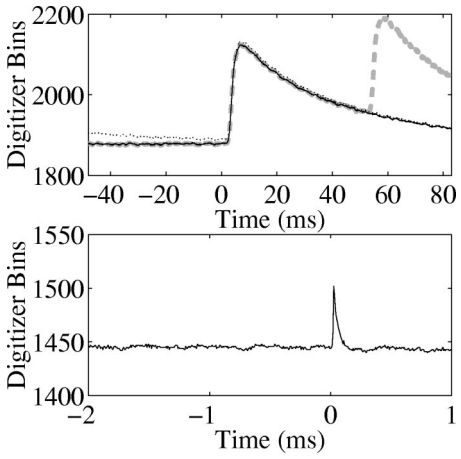

FIG. 12. Typical BLIP phonon-channel (top) and ionization-channel (bottom) pulse shapes, with times shown relative to the trigger time. Overlaid on the phonon pulse shape (solid) are examples of how the pulse might look with pre-trigger pile-up (dots) or post-trigger pile-up (gray dashes). Traces shown are from the BLIP 4 phonon sensor 1 and the inner-electrode ionization channel for a neutron-calibration event with $E_P = 199$ keV and inner-electrode ionization energy $E_{QI} = 23$ keV. The full downloaded phonon trace is shown, but the ionization trace actually extends from 9.8 ms before trigger to 3.3 ms after trigger.

the event ''delay''—the position of the global trigger time relative to the particle interaction, as determined using the detector that gave rise to the global trigger. In the vast majority of events, any multiple scattering occurs on time scales much shorter than the pulse rise times, so it is reasonable to speak of a single particle-interaction time. Once this delay is determined (see Sec. III A), the pulse energy is fit using templates, as described in Sec. III B. These energies are calibrated daily, as described in Sec. III C.

A. Determination of the event delay

Calculation of the delay is done using optimal (Weiner) filtering on the triggering detector [34,53]. If a trace baseline is below the digitizer range, the event is not fitted. For a trace with its peak above the digitizer range, a simplified delay algorithm, which takes advantage of the fact that the start of a large pulse is easy to find, is employed.

If the event's global trigger is an ionization trigger, the calculation is done on the ionization pulse summed over both electrodes, and the trigger time is used for correlating with the veto. If the event is a phonon trigger, first the delay of the average of the two phonon channel pulses is calculated, using a time-domain convolution. Because the phonon pulses have a 5-ms rise time, this delay does not provide a sufficiently precise time-offset estimate to allow correlation with the veto—the veto-trigger rate is ~ 6 kHz, making accidental coincidences too frequent. Instead, the optimal-filter convolution is performed on the ionization traces over a search window restricted by this phonon delay. If no above-threshold pulse exists, the search finds a noise excursion. In the case of a phonon trigger, the widths of the search windows for the phonon and ionization signals are 14.4 ms and 1.6 ms, respectively, large enough that pulses above noise are not found near the window edges.

The delay determined in the above way is used as the time offset in the fitting algorithm for the pulses in all the detectors. It is also used to determine the nearest veto hit. Phonon-trigger events are characterized as veto-anticoincident if there is no veto hit within 25 μs of the time of this inferred delay. Ionization-trigger events are veto-anticoincident if there is no veto hit in the 25 μs before the event trigger.

B. Pulse-energy fitting

Once the delay is determined, the pulse energy is fit using templates. For each channel, a template is built by averaging a number of ionization-triggered pulses. Pulses with energies of 100–200 keV are used to ensure a high signal-to-noise ratio while being low enough in energy to be unaffected by pulse-shape variations with energy. To form templates for the shape of the ionization crosstalk, events with energy only in a single electrode are used. It is necessary to build different templates for each detector and channel because of pulse-shape variations. In the phonon channels, variations are caused by small differences in thermistor properties and detector heat sinking. Variations in the ionization pulse shape occur because of differences in feedback-component values and amplifier open-loop gains.

For the phonon pulses, linear template fits are performed, minimizing the χ^2 defined by

$$\chi^2 = \sum_{i=1}^{N} \frac{|V_i - V_0 s_i|^2}{\sigma^2} \tag{5}$$

where V_i are the ($N = 2048$) digitized data samples, s_i is the pulse-shape template, V_0 is the fitted pulse amplitude, and σ is the rms noise per sample. In practice, additional linear terms are included (a baseline offset and an arbitrarily normalized exponential with time constant fixed to the known pulse fall time to fit the tail of a possible previous pulse), but this simplified description well summarizes the method. Minimization with respect to V_0 yields

$$V_0 = \frac{\sum_{i=1}^{N} \frac{V_i s_i}{\sigma^2}}{\sum_{i=1}^{N} \frac{s_i^2}{\sigma^2}}. \tag{6}$$

The χ^2 of the fit is incorrectly normalized because correlations in the noise between time samples are not taken into account. Cuts based on the χ^2 values are therefore formed empirically, ignoring the overall normalization.

For the ionization traces, it is advantageous to use optimal filtering to calculate the fit energy because of the significant frequency structure of the noise of the ionization channels (due to FET $1/f$ noise, 60 Hz pickup, and pickup of 1 kHz and harmonics from the thermistor bias). Optimal filtering calculates the pulse fit in frequency space, where frequency components with a low signal-to-noise ratio are deweighted to minimize their effect on the fit. The optimal time-offset and energy estimators are given by the time and the value of the peak of the convolution of the optimal filter with the trace. The time offset provides the phase factor to apply to the template in frequency space to allow calculation of the χ^2 in frequency space, where it can be correctly normalized because noise components at different frequencies are uncorrelated. A complication arises because of cross-talk between the inner and outer ionization channels of a single detector. Each ionization channel's trace is the sum of its own pulse and a cross-talk component whose amplitude is proportional to that of the pulse in the other channel. There is an analogous matrix equation for the χ^2 in this case, which fits both ionization channels at once [34].

C. Energy calibrations

Due to drifts in both refrigerator base temperature and the electronics, the phonon energies fit by the above procedure exhibit slow drifts with time. Although the ionization energies do not drift with time, discrete events such as cycling of power on the front-end electronics crate can cause changes in the ionization calibration. It is necessary to perform an absolute, time-dependent calibration to correct these changes.

The energy E_Q of the ionization channels is calibrated for large blocks of time (days to weeks) using the 511 keV positron-annihilation line, which appears during normal low-

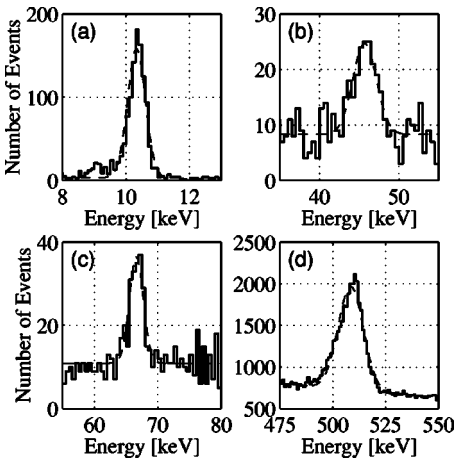

FIG. 13. Spectral lines visible during low-background running, in recoil energy E_R, summed over all four Ge detectors. Gaussian fits are shown as dashed curves. (a) Line at 10.4 keV from internal Ga, using phonon sensors. (b) Line at 46.5 keV from ^{210}Pb, evident in events with energy in the outer electrode only, using the phonon sensors. (c) Line at 66.7 keV from ^{73m}Ge, using phonon sensors. (d) Line at 511 keV from positron annihilation, using ionization sensors.

background running. To account for phonon drifts on scales longer than a day, the overall energy scale of each phonon sensor is calibrated against ionization using the prominent bulk electron-recoil band and the relation $E_P=[1+(eV_b/\epsilon)]E_Q$. To account for phonon drifts due to temperature drifts over shorter time scales, a simple linear correction is made to the phonon pulse height based on the phonon-lockin dc-reference measurement of each thermistor's average resistance, made every 10 s. To first order, the phonon pulse height is linear in deviations of the thermistor resistance due to thermal drifts. The correction is calibrated using phonon-pulser events of known energy. Occasionally, large temperature excursions drive a phonon sensor out of the range for which the correction is calibrated; the detector is considered to be dead during such periods. Success of the energy calibration is demonstrated by the appearance of low-energy spectral lines (see Fig. 13) in the low-background data set described below.

IV. Ge BLIP DATA SET

Between November 1998, and September 1999, 99.4 raw live days of low-background data were obtained using 3 of 4 165 g Ge BLIP detectors. Raw live days denotes the live time of the data-acquisition (DAQ) system, before any cuts are made, excepting periods when the raw data are discarded due to obvious problems. Figure 14 shows the integrated live time for which the DAQ was taking low-background data (i.e., excluding grounding and calibrations). The largest slope is $\sim$0.6 live day/real day; periods of significant dead time are labeled in the figure. During stable low-background running, the dead time consists of time for cryogen transfers ($\sim$10%), detector grounding ($\sim$10%), phonon pulser calibrations ($\sim$5%), and DAQ dead time ($\sim$15%).

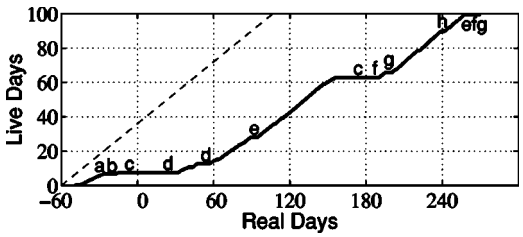

FIG. 14. Cumulative time waiting for a trigger. The dashed line has a slope of 0.6, the maximum observed slope during stable running. The origin of the horizontal axis is January 1, 1999. Labeled periods of significant deadtime were due primarily to (a) computer problems and work, (b) slow pulses (see [34] for details), (c) refrigerator warm ups, (d) electronics work, (e) neutron calibrations, (f) low-bias studies, (g) photon calibrations, and (h) pump failure.

A. Calibrations

As shown in Fig. 14, *in situ* detector calibrations with external photon and neutron sources were performed during the 1999 Ge data run. These calibrations are used to help determine cut efficiencies, as described in Sec. IV C, and to estimate particle-misidentification rates and other possible systematic errors in the analysis of the low-background data.

1. Neutron calibrations

In order to provide nuclear-recoil events that mimic WIMP interactions, a ^{252}Cf-fission neutron source is placed on the top face of the scintillator veto. Because the neutrons emitted by this source have such low energies (see, e.g. [54]), the top layers of polyethylene inside the shield are removed to permit the neutrons to penetrate to the cryostat. With the source and shielding in this configuration, the data set is dominated by neutrons, making the total event rate about 3 times higher than during low-background data taking. In all other ways, the data-taking conditions are as usual. The source activity is known to $\sim$5% accuracy, so the absolute normalization of the spectrum is well determined. The overall cut efficiency, determined by the methods discussed in Sec. IV C, is smaller than for the low-background data because the higher event rate significantly increases the amount of event pileup.

2. Photon calibrations

The photon calibration is performed by inserting a ^{60}Co source through a small, pluggable hole in the lead shield. ^{60}Co emits two high-energy photons, at 1173 keV and 1332 keV. These photons Compton scatter in the material surrounding the detectors, resulting in a secondary photon spectrum similar to the expected radioactive backgrounds. The photons yield a large sample of bulk electron recoils with $\sim$3% surface electron recoils. Although some surface events arise from electrons ejected from surrounding materials, simulations indicate that most low-energy surface events are due to electrons kicked through the dead layer (and then out of the detector) by high-energy photons Compton scattering *inside* a detector.

Because the calibration results in many high-energy events, whereas the WIMP search uses only low-energy

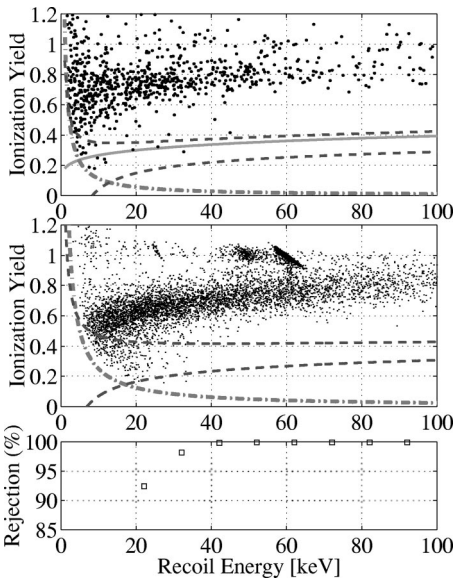

FIG. 15. Electron calibration data. Hyperbolic dot-dashed lines: mean ionization-search thresholds. Solid curves: mean centers of nuclear-recoil bands. Dashed curves: mean nuclear-recoil-acceptance regions. Top: 1999 run electron-calibration set consisting of 407 veto-anticoincident events tagged as multiple scatters in BLIP 3 and BLIP 4. Middle: Data from external ^{14}C source data taken with test device ABL1 with a source-side electrode at positive bias. Bottom: Rejection efficiency for the test device.

events, a hardware trigger veto rejects events with recoil energy $E_R \gtrsim 100$ keV during the photon calibration. The calibration data are analyzed in the same way as the normal data stream. As with the neutron-calibration data, a larger fraction of events are cut due to pileup. This larger fraction is not a concern because the photon misidentification is determined by beginning with a set of events that pass all data-quality cuts and then calculating the fraction that also pass the nuclear-recoil-acceptance cut. The efficiency of the data-quality cuts has no effect, since no data-quality cuts depend on the ionization yield.

3. Electron calibrations

Unfortunately, *in situ* calibrations with external electron sources are not practical because of the substantial material forming the cold volume. Furthermore, BLIPs 3–6 were never tested with an external electron source in the laboratory. Small devices prepared with variants of the electrode have been tested with an electron source (see Fig. 15), but no laboratory electron calibration was performed with the exact electrode structure used on the detectors.

The photon calibration contains a very small fraction of electrons, $\sim 0.7\%$ in the 10-to-100-keV range according to Monte Carlo simulations. The typical number of events observed in this energy range during the calibration is ~ 9000 per detector. Therefore, only ~ 60 electrons are expected per detector, insufficient for placing a useful limit on electron misidentification.

The veto-anticoincident data provide an electron calibration because BLIP 3 appears to be heavily contaminated with an electron source that results in clear electron bands in BLIPs 3 and 4. The contamination likely consists of ^{14}C atoms from a leaking ^{14}C source to which the detector was exposed during an attempted laboratory calibration. Low-energy (10–100 keV) veto-anticoincident multiple-scatter events between BLIP 3 and BLIP 4 appear to be dominated by this electron ''source'' on the surface of BLIP 3. Figure 15 shows ionization yield vs recoil energy in the two detectors for the calibration data set. The surface events form a clear band in ionization yield, similar to that seen in a test device with α-Si contacts. The bulk of the events are concentrated at low recoil energy, so this data set probes energies where electron misidentification is worst.

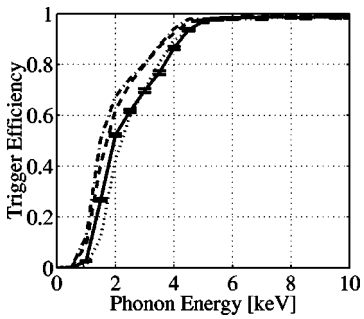

FIG. 16. Efficiency of hardware phonon trigger vs phonon energy E_P, for BLIP 3 (solid line), BLIP 4 (dashes), BLIP 5 (dotted-dashes), and BLIP 6 (dots). Statistical uncertainty (1σ), shown for BLIP 3, is similar in the other detectors. These results are averaged over the entire data set; the slight residual trigger inefficiency above 5 keV is dominated by a four-week period with slightly worse trigger filters.

B. Hardware and analysis thresholds

For all events, every detector channel is digitized and trace fits done. The hardware-trigger efficiency for each detector can be measured using events in which any of the other detectors was the first to trigger. The trigger efficiency for a given detector as a function of energy is defined as the fraction of such events for which that detector's trigger is found in the post-trigger history. This analysis is done separately for the phonon trigger as a function of phonon energy and for the ionization trigger as a function of ionization energy. To ensure good energy estimates, this calculation is done on the set of events passing all data-quality cuts (note data-quality cuts do not require that events are single scatters; see Sec. IV C). Figure 16 shows the phonon-trigger efficiency as a function of phonon energy.

For phonon-trigger events, it must be determined whether the ionization signal is due to amplifier noise or to real ionization. Because the phonon pulses have ~ 5 ms rise times, for phonon-trigger events we search for ionization pulses inside a 1.6-ms-wide time window. An optimal-filter algorithm picks out the largest peak in the window. Random-trigger events are used to determine, on a day-by-day basis, the ionization search threshold above which the ionization is unlikely to be just noise. The standard optimal-filter algorithm finds the delay and energy for the random-trigger events. The resulting energy distribution is approximately Gaussian but

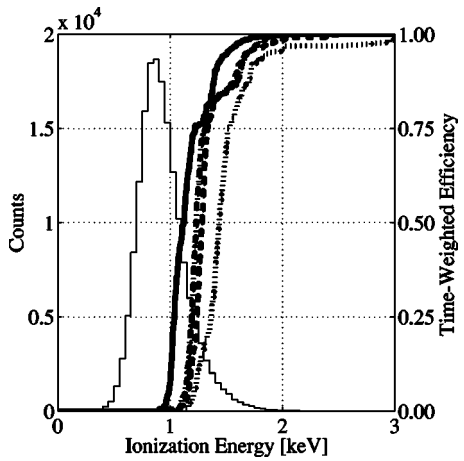

FIG. 17. Thin solid line: Distribution of summed ionization energy in BLIP 6 for random triggers as determined by the ''sliding'' noise fit. Also shown are the data-averaged ionization search threshold efficiency curves for BLIP 3 (thick solid line), BLIP 4 (dashes), BLIP 5 (dotted-dashes), and BLIP 6 (dots).

is offset positively from zero, is narrower than the zero-delay noise distribution, and has a non-Gaussian tail to high energy:

$$P(E)=M[\mathrm{erf}(E,\sigma_E)]^{M-1}\frac{1}{\sigma_E\sqrt{2\pi}}\exp\left(-\frac{E^2}{2\sigma_E^2}\right) \quad (7)$$

where M is the number of samples in the search window and σ_E is the width of the zero-delay noise distribution [34]. A histogram of energies yielded by the sliding noise fit for random triggers is shown in Fig. 17, together with the data-averaged ionization search threshold efficiencies for each of the four detectors. Events with no real ionization are called ''ionization-noise'' events.

Only events above the ionization-search threshold are included in the analysis because two classes of events otherwise could mimic WIMP events. Muon-induced events without a clear ionization pulse cannot be vetoed because the slow phonon timing information is too poor to allow correlations with the muon veto. Thermal events, such as detector displacement in its support, yield phonon energy but no ionization, and hence could also be mistaken for WIMP events were no ionization threshold applied.

Although the phonon-trigger efficiency is $\sim$100% for phonon energies $E_{\mathrm{P}}>5$ keV, an analysis threshold is placed at recoil energy $E_{\mathrm{R}}=10$ keV for two reasons. First, for energies $E_{\mathrm{R}}\lesssim 10$ keV the efficiency for identifying nuclear recoils decreases precipitously as energy decreases because of the fraction of nuclear-recoil events producing less ionization than the ionization-search threshold. Below 10 keV, the uncertainty in our determination of this efficiency would make interpretation of the number of identified nuclear-recoil events unreliable. Second, at these same energies, the expected contamination of the nuclear-recoil band with electron-recoil events appears to be non-negligible.

Analysis is further restricted to events below 100 keV because the nuclear-recoil efficiency above 100 keV is not well determined. This uncertainty arises simply because there are so few neutron-calibration interactions above 100 keV that the position of the nuclear-recoil band cannot be determined. This restriction does not significantly degrade the detectors' sensitivity to WIMPs or to background neutrons because both types of particles produce recoil-energy spectra that are approximately exponential with $\langle E_{\mathrm{R}}\rangle \lesssim 30$ keV.

C. Software cuts

To prepare the data for a search for WIMP-induced nuclear recoils, a number of data-quality cuts are made, as described in Secs. IV C 1–IV C 3. The goals of these cuts are to remove pileup, to remove periods of high noise or trace-baseline wandering, and to select only those events where the pulse fits are of sufficient quality to ensure the accuracy of the energy estimate and hence the ability to reject electron-recoil background events. Additional ''physics'' cuts preferentially reject background events, as described in Secs. IV C 4–IV C 8. All cuts other than the nuclear-recoil cut were set after initial examination of the data. In order to minimize the potential for introducing bias, these cuts were set without regard to the number of events passing the nuclear-recoil cut, as described below. In particular, the data-quality cuts were set using a random 10% of the data with no other cuts applied. The veto-anticoincidence cut (see Sec. IV C 4) was set from a random 10% of the data with only the data-quality cuts applied.

1. Pre-trigger-trace-quality cuts

A number of cuts are made using information not about the events, but only on the quality of the setup prior to the event trigger. Periods of known poor energy resolution are discarded. For the early part of this run, problems with the detectors' electronics were the dominant cause of such cuts. Detectors failing these cuts are discarded for the periods in question, but events in other detectors during these periods are not cut. These cuts remove 5–10 % of the low-background data for each detector, slightly decreasing the expected fraction of neutron-induced events that multiply scatter between detectors. A detector is considered to be ''live'' for the events for which it passes these cuts.

Additional cuts are made on pretrigger-trace quantities to ensure the traces are free of pileup, the pulses are within the digitizer window, and the noise environment is reasonable. First, the mean pretrigger baselines of all channels are required to lie in a range so that an event of interest ($<$100 keV) would not saturate the digitizers. Second, the standard deviations of the pretrigger baselines are required not to be too large. These cuts remove events with pretrigger pileup, high phonon noise, or low-level baseline wandering that increases the baseline noise. Any of these problems may compromise the energy measurement. Third, the detector temperatures, as measured by the phonon-lockin dc reference voltages, are required to be in the range for which the linear ''dc-reference correction'' discussed above (Sec. III C) is calibrated. For an event to be accepted, all live detectors must pass all these cuts.

TABLE I. Pre-trigger-trace-quality cut efficiencies for the four detectors, as measured by three different methods. The total live time before any cuts is 99.4 live days. As noted in the text, the fraction of pulser events passing pretrigger cuts accurately measures the efficiency, while the estimates based on fractions of events should be systematically low, and the estimates based on fractions of live time should be systematically high.

Pre-trigger cut efficiency	BLIP 3	BLIP 4	BLIP 5	BLIP 6
Fraction of data live time	0.79	0.77	0.82	0.83
Fraction of pulser events	0.76	0.73	0.78	0.78
Fraction of data events	0.71	0.69	0.75	0.75

The calculation of the efficiency of these combined pre-trigger cuts is straightforward because the cuts have no dependence on the event characteristics. The efficiency is given simply by the fraction of ionization-pulser events passing the cuts (see Sec. II A 3). Furthermore, both lower and upper bounds on the pretrigger-cut efficiency may be calculated easily from the data itself. The live time of an event is defined as the time waiting for the trigger after the trigger is armed. An upper bound on the pretrigger-cut efficiency is given by the ratio of the sum of the live time of the events passing the cut set to the sum of the live time of all events. If the experiment were live for all the live time preceding events that pass the pretrigger cuts, then this ratio would yield the cut efficiency. Since the experiment may actually be dead for part of this time (e.g., time recovering from a high-energy deposition in one or more detectors), this method yields an upper bound on the efficiency. A lower bound on the pretrigger-cut efficiency is given by the fraction of events passing the cuts. If the trigger rate were constant over the entire run, then the fraction of events passing the cut would naturally yield the cut efficiency. Because more triggers occur during periods when events are more likely to fail the pretrigger cut (e.g., due to periods of high noise, which can induce triggers), this estimate yields a lower bound on the efficiency. Table I displays the efficiencies together with these bounds for the final all-detector pre-trigger trace-quality cuts.

2. Post-trigger pile-up cuts

Because the phonon pulses for the BLIP detectors are considerably slower than the ionization pulses, events with accidental additional hits on the ~80-msec time scale of the phonon pulse could result in additional phonon energy without additional ionization energy on the shorter time scale of the ionization pulse, potentially mimicking the signature of nuclear recoils. To avoid contamination by these events, additional care is taken to reject detectors with evidence of pile-up. Events with discernible pulses in the post-trigger phonon digitization window (as evidenced by a second peak in the pulse larger than the triggering peak) are rejected. To reject accidental pile-up with small delays (<10 ms) that may not result in a distinguishable second phonon pulse, we also reject detectors with additional accidental ionization triggers more than 50 μs before or more than 300 μs after

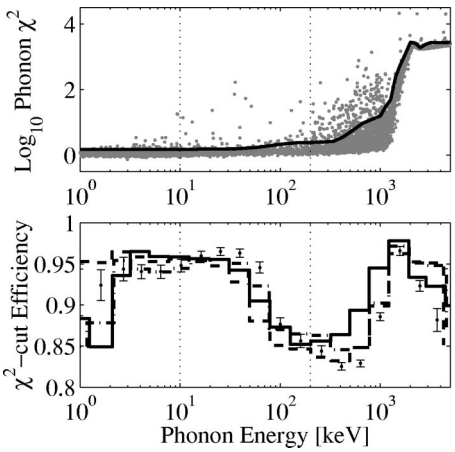

FIG. 18. Top: Typical phonon-pulse fit χ^2 vs phonon energy. The phonon χ^2 is a reduced χ^2 for approximately 2000 samples, but it is not properly normalized. The line on the plot indicates the position of the cut calculated by the automated algorithm. Bottom: Efficiency of phonon-χ^2 cut vs phonon energy for the four BLIP detectors. Error bars are shown for BLIP 3 data only. Curves indicate data for BLIP 4 (solid), BLIP 5 (dashed), and BLIP 6 (dotted-dashed). For both plots, the vertical dotted lines indicate the approximate phonon energies corresponding to the 10–100 keV recoil-energy analysis region.

the primary trigger (additional triggers very near the primary trigger may be due to double triggering in the electronics or multiple scattering). Further cuts (described in Sec. IV C 3) remove the remaining events that are contaminated with pile-up. All these cuts remove only the detector(s) whose events are contaminated with pile-up; events in detectors without pile-up are not cut.

The efficiency ϵ_p of the pile-up cut can be calculated directly from the trigger rate by assuming that the occurrence of a second event of any energy causes an event to fail the cut. This estimate is a good one at low energies—if the first event is below 100 keV, the second event is likely to be more energetic simply because most of the trigger rate comes from events above 100 keV. This efficiency ϵ_p is given by the accidental rate for a second event to appear in the 10 ms pretrigger dead period or in the 83 ms phonon post-trigger period, which is

$$1-\epsilon_p = 0.093\text{s}\times R \tag{8}$$

where R is the measured single-detector trigger rate. The typical single-detector trigger rate is 0.33 Hz, so $\epsilon_p \approx 0.97$. This result agrees well with the fractions of events that pass the cut, $0.96 < \epsilon_p < 0.98$ for the four detectors.

3. Trace-quality cuts

In order to ensure rejection of all events with pile-up, and in order to discard pulses that may result in misestimated energies, cuts are made on the pulse-shape χ^2 values. Pulse-shape templates are formed to match the shapes of low-energy pulses to ensure best energy resolution for such events. At high energy, as shown in Fig. 18, pulse-shape changes result in severe deviation of χ^2 from its low-energy

value. The slow rise away from the low-energy χ^2 value is due to minor pulse-shape nonlinearity as the energy is increased. The abrupt change at ~ 1 meV coincides with the beginning of digitizer saturation. Furthermore, the χ^2 distributions change on time scales of one to a few days, as the phonon pulse shape changes due to thermal drifts. An automated empirical approach is taken in defining the phonon-χ^2 cut as a function of energy separately for each day of data [34]. Figure 18 shows a typical cut determined by this automated technique.

The efficiency of the cut in each energy bin is estimated simply as the fraction of events that pass it. Although the cut efficiency varies over time, the efficiency calculated from the data set as a whole should correctly incorporate the variations. For example, a period with a low cut efficiency is weighted according to the total number of events in the set before the χ^2 cut, which is proportional to the live time of the period, providing the correct weighting. The prior cuts remove extraordinary periods, so this procedure is valid. Furthermore, the assumption is conservative in that it can only underestimate the efficiency. For example, if a trigger outburst is left in the data set from which the efficiency is calculated, then it is overweighted because it has too many events. The efficiency for such a period is lower than is typical because of the higher noise. Thus, the mean efficiency is decreased by such a period.

The efficiency of the phonon-χ^2 cut as a function of phonon energy is shown in Fig. 18. The efficiency has structure that arises mainly from the fact that, at a few hundred keV, the χ^2 distribution broadens and exhibits a tail. While the shape of the efficiency function may appear strange, it is correct—a more stringent cut is made at higher energy, giving a lower efficiency.

Because the ionization χ^2 is well behaved, a cut on ionization χ^2 is barely necessary. A very liberal cut is made, accepting all events that do not saturate the digitizers.

An additional trace-quality cut is made because low-energy phonon-trigger events could in principle trigger so late that the ionization pulse lies before the downloaded section of the digitized trace. Furthermore, for data from the first part of the run, the ionization-search algorithm was allowed to fit a pulse with falling edge at the very beginning of the digitization window, typically resulting in a poor energy estimation. Such events are rejected by cutting events with ionization-pulse start times too close to the beginning of the digitization window. The length of the ionization pretrigger trace was increased from about 6 ms to 9 ms midway through the data set; therefore, two cut values are used: -5.5 ms for the 6 ms data and -8 ms for the 9 ms data. These two cut values are indicated in Fig. 19.

As is seen in Fig. 19, even with the cut at -5.5 ms, a significant number of ionization pulses should be missed only for phonon energies $E_P < 8$ keV. For this reason, although the efficiency of this cut is calculated, it has a small effect for the analysis, which considers only events with recoil energies $E_R > 10$ keV.

4. Veto-anticoincidence cut

For dark-matter analysis, a cut is made to remove events coincident with activity in the veto. Because of the high veto rate $R_v \approx 6$ kHz, narrow veto windows in time must be used to minimize the rate of accidental coincidences. If an event's global trigger is an ionization trigger, the veto-coincidence window extends only before the trigger time, because an ionization trigger may occur only after the particle interaction that caused it. An ionization-trigger event with any veto hits in the 25 μs before the detector trigger is considered veto-coincident. This window size was determined by choosing the point where the distribution of last veto-trigger times deviates from the $\tau = 150$ μs background exponential (see Fig. 20). This exponential is due to background photons emitted following thermal-neutron capture on the polyethylene moderator.

For an event with a phonon trigger but no ionization trigger, the veto-coincidence cut is different. As described in

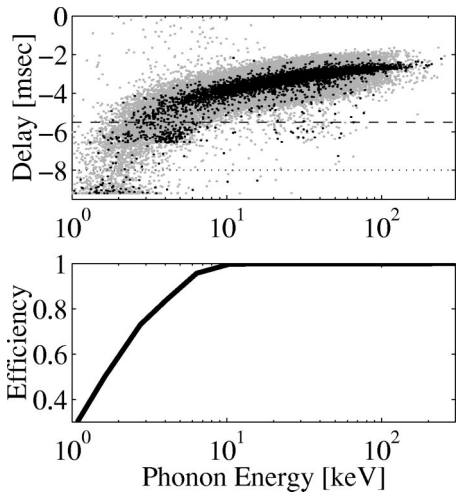

FIG. 19. Top: "Ionization delay" vs phonon (*not* recoil) energy for a random one-tenth of the data, showing the time walk of the phonon trigger. The ionization delay is the time of the ionization pulse relative to trigger time, with negative values indicating the ionization pulse occurred before the trigger. The dashed and dotted lines indicate the position of the ionization-delay cut; the cut at -5.5 ms is used for data with 6 ms of pretrigger information and the cut at -8 ms for data with 9 ms of pretrigger information. Dark (light) dots indicate events with ionization above (below) the ionization-search threshold. Bottom: Efficiency of the cut vs phonon energy in the triggering detector.

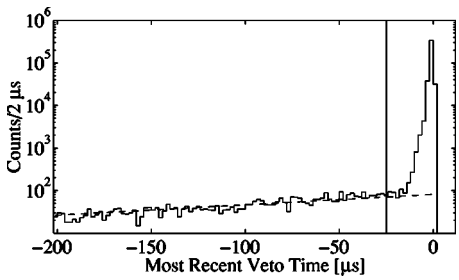

FIG. 20. Distribution of the last veto-trigger times for ionization-trigger events for a random 10% of the data. The exponential background distribution has a slope corresponding to $\tau = 150$ μs (shown as dashes). The 25-μs coincidence window is indicated.

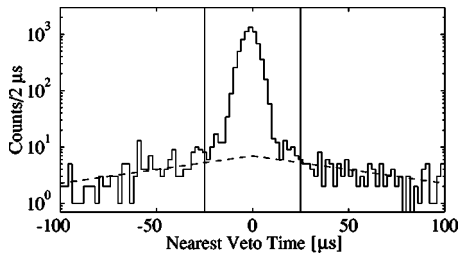

FIG. 21. Distribution of the nearest veto-trigger times for phonon-trigger events, relative to the time of the ionization pulse, for events above the ionization-search threshold. The width of the peak is dominated by the uncertainty on the reconstructed time of the ionization pulse. The exponential accidental distribution is shown as dashes. The ± 25-μs coincidence window is indicated.

Sec. III A, a search for a pulse in the ionization trace is performed for phonon triggers. If an ionization event is found, its time can be compared to the veto-trigger history. The uncertainty on the time of the ionization pulse makes it necessary to search for the nearest veto hit not only before the inferred time of the pulse, but also after it. The distribution of nearest veto-trigger times for phonon triggers with an ionization pulse found is shown in Fig. 21. Based on the points where the distribution deviates from an exponential accidental distribution, a cut window of ± 25 μs is set. For phonon triggers without ionization, the uncertainty on the event time is comparable to the average time between veto events, making vetoing useless. Primarily for this reason, all events without ionization pulses are discarded.

The efficiencies of the veto-anticoincidence cuts are determined by the fraction of random-triggered events that they reject averaged over the course of the run. Using the random-triggered events accurately takes into account variations in veto rate over the course of the run. The resulting efficiencies, 87% for ionization triggers and 75% for phonon triggers with ionization found, agree with the measured average veto-trigger rate $R_v \approx 6$ kHz. For ionization triggers, the probability that an accidental coincidence occurs is $1-\exp(-6\ \text{kHz} \times 25\ \mu\text{s}) = 0.13$, yielding an efficiency of 0.87. For phonon triggers with ionization found, the window is ± 25 μs, giving an efficiency of 0.75.

5. Removal of thermistor-contained events

Particle interactions may occur in the thermistors themselves, resulting in little or no ionization energy. The resulting phonon pulses in the two thermistors are very different from crystal-interaction pulses. When fitted with a standard pulse template, such events result in extremely different pulse heights P_1 and P_2 for the two thermistors. To reject detectors with interactions in one or the other thermistor, a cut rejects detectors with events for which $|(P_1-P_2)/(P_1+P_2)|>0.2$. As shown in Fig. 22, this cut results in a negligible loss of efficiency for events in the crystal.

6. Removal of BLIP 3

The rate of low-ionization-yield events in BLIP 3, the top detector of the 4-detector stack, is significantly higher than the rates in the other detectors (230 $\text{kg}^{-1}\,\text{d}^{-1}$ as compared to 50 $\text{kg}^{-1}\,\text{d}^{-1}$ for the other detectors). BLIP 3 was the prototype detector for these four BLIPs; it suffered repeated processing steps during development of a new electrode-fabrication method [34], so its electrodes may have been damaged during processing. Moreover, exposure to an external ^{14}C source recently found to be leaky appears to have contaminated BLIP 3's surface with ^{14}C. For this reason, BLIP 3 is discarded for dark-matter analysis. BLIP 4 also shows an elevated rate of low-yield events contained in the inner electrode, likely due to electrons emitted by the ^{14}C contaminant on BLIP 3. As shown in Fig. 23, there is good separation between BLIP 4's low-yield band and the nuclear-recoil-acceptance region. Because of this good separation, BLIP 4 is included in the experiment's fiducial volume along with BLIP 5 and BLIP 6.

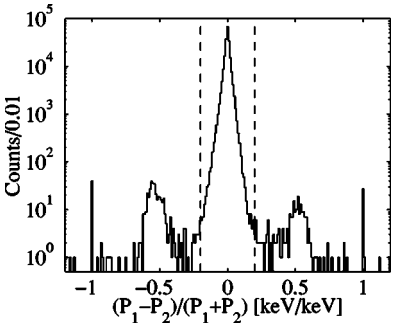

FIG. 22. Histogram of phonon partition. The dashed lines indicate the acceptance region; events failing the cut are dominated by interactions in the NTD thermistors.

7. Fiducial-volume cut

As described in Sec. II A, the detectors have radially segmented electrodes to allow rejection of events due to par-

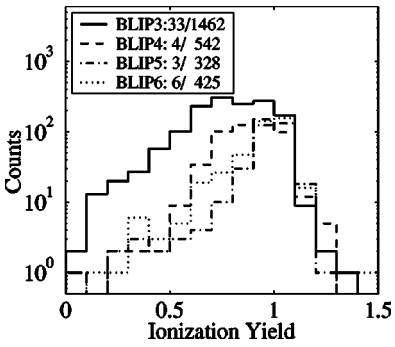

FIG. 23. Distributions of ionization yield Y for veto-anticoincident single-scatter events with recoil energies between 10–100 keV, fully contained in the inner electrode of BLIP 3 (solid line), BLIP 4 (dashed line), BLIP 5 (dotted-dashed line), or BLIP 6 (dotted line). BLIP 3's high event rate, particularly for yields slightly too high to be nuclear recoils ($Y \approx 0.5$), indicates its contamination by a source of low-energy electrons. Although BLIP 4 shows a high rate of events with $Y \approx 0.8$, its rate just above the nuclear-recoil acceptance region is similar to that of BLIP 5 and BLIP 6. The legend lists the number of events that fall in the nuclear-recoil acceptance region for each detector as a fraction of the total number of events in that detector.

ticles incident on the sides of the detectors, which are less shielded. The two electrodes result in three categories of events. ''Inner-electrode-contained'' events have an inner-electrode signal greater than 4σ above the noise mean and have an outer-electrode signal within $\pm 2\sigma$ of the noise mean. The strict requirement on the inner-electrode signal ensures that events are not classified as inner-electrode-contained due to noise fluctuations. ''Outer-electrode-contained'' events have an inner-electrode signal less than 4σ above the noise mean and an outer-electrode signal greater than 2σ above the noise mean. Finally, ''shared-electrode'' events have an inner-electrode signal greater than 4σ above the noise mean, and an outer-electrode signal greater than 2σ above the noise mean. The shared-electrode events arise either due to interactions in the physical volume near the break between the inner and outer electrodes, or due to multiple scatters under each electrode. Here, the noise mean and standard deviation are given by the noise parameters calculated from random-trigger events on a day-by-day basis.

The fraction of the detector volume accepted by the three volume cuts is determined using the relative numbers of calibration neutrons passing each cut at high energy, where thresholds have a reduced effect. The fractions averaged over 20–100 keV are 47%, 22%, and 31% (with $\pm 2\%$ statistical uncertainty) for the inner-electrode, shared-electrode, and outer-electrode volumes, respectively.

Two straightforward corrections must be made. First, according to Monte Carlo simulation of the neutron calibration data, 9% of neutrons yielding 20–100 keV recoil energy scatter once under each electrode of a given detector, yielding a shared event. Second, the simulation shows that the probability of a neutron interacting in the outer electrode is 14% higher than expected from the volume fraction, simply due to self-shielding [55] (WIMPs of course interact too weakly to show a shielding effect or to multiple scatter). The results for the inner-, shared-, and outer-electrode fractions are therefore 46%, 19%, and 35%. The inner electrode nominally contains 56% of the detector volume, so these numbers are consistent with the shared volume being geometrically equally divided between the inner and outer electrodes, as expected. Systematic uncertainty on the fiducial-volume fractions, due to possible inaccuracies in the Monte Carlo simulation, is estimated at 3% [55]. At low energies, the importance of thresholds makes the calculated fiducial volume more dependent on how ionization is shared between the two electrodes for events in the shared volume. For this reason, at low energies the uncertainty on the efficiencies of the fiducial-volume cuts is $\sim 10\%$.

Calibration and low-background data are used in order to determine whether events in the outer electrode and events shared between the two electrodes should be rejected. Histograms of ionization yield, shown in Fig. 24, suggest that the outer-electrode events should be discarded. The photon calibration indicates that the photon misidentification is ~ 50 times higher for outer-electrode events than for inner-electrode or shared events. Beyond this, the much flatter Y distributions for the outer-electrode data indicate that, though the outer-electrode electron rate is not significantly different from the rates seen for the inner-electrode and shared cuts, the electron-misidentification fraction is likely to be much worse.

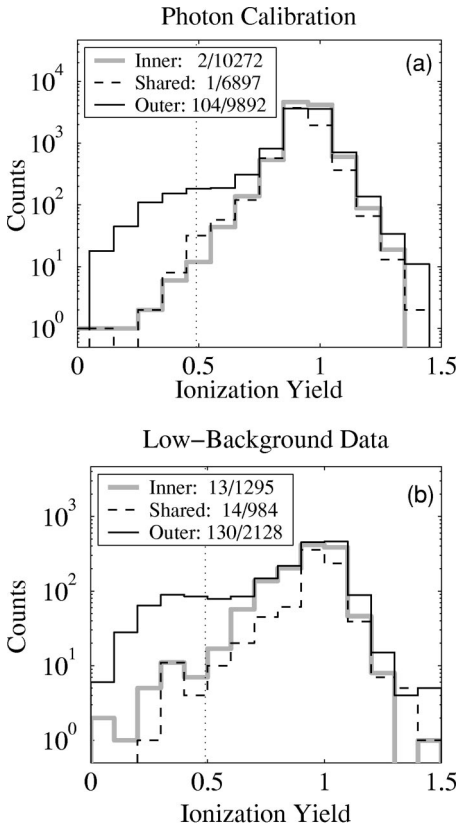

FIG. 24. Histograms of ionization yield Y for interactions with 10 keV$<E_R<$100 keV in BLIP 4, 5 or 6 in (a) photon-calibration data and (b) veto-anticoincident low-background data. The vertical lines indicate the maximum position of the nuclear-recoil-acceptance region for any energy or detector. The legend gives the number of events in the nuclear-recoil-acceptance region as a fraction of the total number of events; the former number is determined using the fully energy-dependent acceptance region, not just the line shown in the plots. The high fraction of outer-electrode photon-calibration events in the nuclear-recoil acceptance region, together with the high fraction of low-background events with yields slightly too high to be nuclear recoils ($Y \approx 0.5$), indicates the outer electrode's poor discrimination against electron contamination. Four (27) of the shared-electrode (outer-electrode) events in the nuclear-recoil acceptance region, and 191 (310) of the events overall, occurred during the 4-V-bias section of the data.

There appears to be no reason to discard the shared-electrode data from most of the run. As shown in Sec. IV D, the shared-electrode electron- and photon-background rates are not significantly higher than for the inner-electrode data set. The photon-calibration data set indicates that the photon- and electron-misidentification fractions for the shared region are no worse than for the inner-electrode region. The Y histograms for the background data corroborate this point. Because both the rates and the misidentification fractions of photons and electrons are not too different for the two regions, the expected rate of misidentified photons and electrons in the two regions should be about the same.

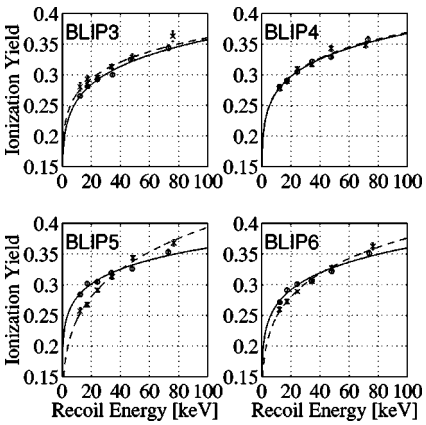

FIG. 25. Nuclear-recoil-line data points and fits for the April (circles and solid curves) and September ($\times$'s and dashed curves) neutron calibrations. For BLIP 5 in particular, the two nuclear-recoil lines are clearly shifted relatively to each other.

However, for a short part of the run, the charge electrodes were biased at 4 V, as opposed to the 6 V bias used for the rest of the run and for all the calibration data. As shown in Sec. IV C 10, veto-coincident data indicate the possibility of worse contamination for the 4 V shared-electrode data than for the 6 V shared-electrode data. For this reason, the 4 V shared-electrode data are discarded.

The original WIMP-search analysis of this data used only events with at least one detector hit fully contained in the inner electrode [18]. For the current analysis, we include all events with any ionization energy in an inner electrode (both ''inner-electrode-contained'' and ''shared'' events), excepting the 4 V shared-electrode data. We will call these events ''QIS'' events. We will also show how the results would change if we enforced the stricter requirement that all events be ''QI'' events, fully contained in the inner electrode. We will use ''QS'' as a shorthand for the shared events.

8. Nuclear-recoil cut

To determine the position of the nuclear-recoil-acceptance region in ionization yield as a function of recoil energy, two neutron calibrations were performed during the 1999 run: one in April, approximately midway through the run, and a second in September, at the end of the run.

The timing of the first neutron calibration was fortunate, as it occurred on April 2, one day before a Stanford-wide power outage that damaged the electronics chain, introducing a nonlinearity in the ionization-energy response. An empirical linearization corrects the nonlinearity using the well-defined band of bulk electron recoils provided by the single-scatter veto-coincident photon data [34]. In spite of this linearization, the nuclear-recoil acceptance region shifts between the pre- and post-April 3 data sets. This shift is apparent in both the veto-coincident-neutron data and the second neutron calibration. To account for this shift, the nuclear-recoil band is defined separately for data before and after the power outage, based on the two neutron calibrations. Figure 25 shows the power-law functions $Y_{\mathrm{NR}}=cE_{\mathrm{R}}^{d}$ that best fit the center of the nuclear-recoil band for the two neutron calibrations. The observed one-standard-deviation width σ_{NR} of the nuclear-recoil band is also parametrized as a function of recoil energy: $\sigma_{\mathrm{NR}}=aE_{\mathrm{R}}+b$. Gaussian distributions described by these parameters provide excellent fits to the distributions in Y of the neutron-calibration events.

A nominal 90% acceptance band (chosen before data-taking began) is given by a region that extends from $Y_{\max}1.28\sigma_{\mathrm{NR}}$ above to $Y_{\min}3\sigma_{\mathrm{NR}}$ below the fit Y_{NR}. For recoil energies below $\sim$10 keV, the band is truncated from below at the ionization yield $Y_{\min}=Q_{\min}/E_{\mathrm{R}}$ corresponding to the ionization-search threshold $Q_{\min}$. The nuclear-recoil efficiency ϵ_{NR} may therefore be calculated for any recoil energy E_{R}:

$$\epsilon_{\mathrm{NR}}=\int_{Y_{\min}(E_{\mathrm{R}})}^{Y_{\max}(E_{\mathrm{R}})}\frac{1}{\sigma_{\mathrm{NR}}\sqrt{2\pi}}\exp\left[\frac{(y-Y_{\mathrm{NR}})^2}{2\sigma_{\mathrm{NR}}^2}\right]dy. \qquad (9)$$

It is also possible to calculate the nuclear-recoil efficiency empirically. A wide ''cleaning cut'' encloses the neutron band and excludes events that are clearly not neutrons. This cut results in a sample dominated by neutrons, except at low energies, where it also accepts ionization-noise events. Not all ionization-noise events are neutrons, so the ''raw'' number of nuclear recoils is overestimated and the efficiency underestimated at energies where ionization-noise events may fall in the nuclear-recoil acceptance region ($<$10 keV). The data are binned in recoil energy, and the fraction of events accepted in each recoil-energy bin is calculated. The empirical efficiency matches the nominal efficiency well at high energies where it should; 88% of events passing the cleaning cut fall within the nominal 90% acceptance region. The small difference between the empirical efficiency and the nominal one gives an estimate of the systematic error on this efficiency.

In order to calculate the efficiency of the nuclear-recoil cut for the low-background data, changes in ionization noise with time (which dominate changes in phonon noise) must be taken into consideration. An increase in ionization noise results in a higher ionization-search threshold, effectively reducing the nuclear-recoil cut efficiency at low energies where the threshold cuts into the nuclear-recoil acceptance region. More significantly, higher ionization noise makes nuclear recoils at all energies more likely to spill out of the nuclear-recoil acceptance region. For the beginning of the run, when ionization noise was worst, this latter effect reduces the efficiency by $\sim$20%. Both effects are included when calculating the expected nuclear-recoil cut efficiency on a day-by-day basis. Also taken into account is the fact that data for part of the run was taken with 4-volt ionization bias, while most of the data used a 6-volt bias, for which ionization noise is more significant.

9. Combining efficiencies

For single-scattering events (such as those caused by WIMPs), combining the above efficiencies to determine the overall efficiency is straightforward. The time variation of efficiencies other than the nuclear-recoil efficiency is generally small and does not appear correlated with the variation

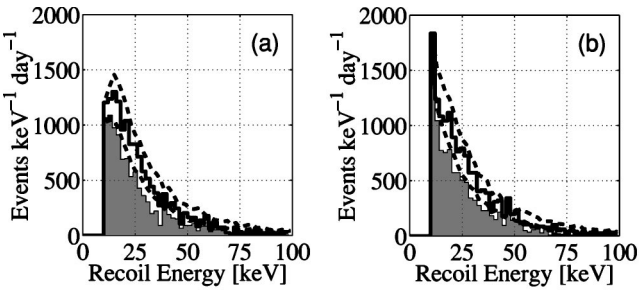

FIG. 26. Observed and simulated recoil-energy spectra, coadded over all four detectors, with no free parameters, for (a) the first neutron calibration, and (b) the second neutron calibration. Solid lines: observed spectra. Dashed lines: simulated, with efficiency corrections applied. The upper spectra are for all QIS nuclear recoils, while the lower, shaded spectra are for all QI nuclear recoils. These same curves, on a logarithmic scale, are shown below in Fig. 39.

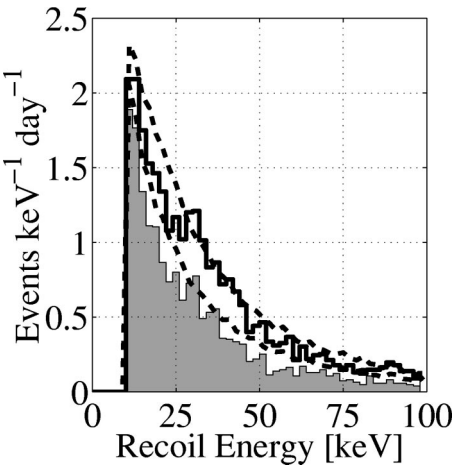

FIG. 27. Muon-coincident-neutron recoil-energy spectra, coadded over BLIPs 4–6, for the entire run, with no free parameters. Solid: observed spectra. Dashed: simulated. The upper spectrum is for QIS nuclear recoils, while the lower, shaded spectrum is for QI nuclear recoils. These same curves, on a logarithmic scale, are shown below in Fig. 39.

of other efficiencies. Therefore, the product of the individual efficiencies yields the total efficiency for each detector. The systematic error due to making the assumption that efficiencies are uncorrelated in time should be $<5\%$. For multiple-scattering events, however, care must be taken because some cut efficiencies for different detectors are correlated for individual events. The χ^2-cut efficiency exhibits no correlations because its energy dependence is dominated by the individual detector noise and pulse-shape characteristics. The nuclear-recoil-cut efficiencies are also uncorrelated, aside from correlations introduced by real physics; e.g., multiple scattering of a neutron. The energy-independent data-quality-cut efficiencies, however, are correlated. An example case of how data-quality cuts introduce correlations is post-trigger pileup. When a detector has post-trigger pileup, its neighbor has a higher-than-random chance of also having post-trigger pileup because the neighbor may be hit by the same particle or by particles produced by the same incident muon or high-energy photon. Therefore, it is necessary to calculate a matrix of the joint data-quality-cut efficiencies, with the probabilities of detectors passing cuts depending on the number of detectors that triggered. These efficiencies are calculated directly from the data.

10. Checks of cut efficiencies

The absolute accuracy of the efficiency calculation can be checked using the neutron calibration. Such a check relies on the accuracy of the neutron Monte Carlo simulation; insofar as the simulation may be less accurate than the calculated efficiencies, this comparison yields only a rough upper limit on the systematic error of the efficiencies. The observed and simulated spectra for the two neutron-calibration data sets are shown in Fig. 26. There are no free parameters in the comparison; the simulation normalization is set by the source activity and the efficiencies calculated from the data. For both calibrations, the simulated spectra are about 10% high at low energies, and are about 50% high at high energies. Moreover, although the low-energy cut efficiencies for the two calibrations are significantly different, both spectra are reproduced by the simulation with similar relative errors after application of the cut efficiencies. For both calibrations, the fraction of events classified as QI is underestimated at low energy, owing to the conservative model that describes how ionization is shared between the two electrodes.

The accuracy of the nuclear-recoil efficiency can also be checked by comparing the simulated and observed spectra for muon-coincident neutrons. As discussed in Sec. II E, these neutrons are produced by muons that interact in the copper cans of the cryostat or in the internal lead shield after passing through the veto. This data set offers the advantage that it is acquired at the same time as the WIMP-search data set, and thus the efficiencies are exactly the same, with the exception that no veto-anticoincidence cut is applied. Figure 27 shows the simulated and observed muon-coincident-neutron spectra for the same energy cuts and event categories as shown for the neutron-calibration data. Similar to the neutron-calibration data, predicted spectra are slightly harder than observed spectra, with simulated spectra about 10% high at low energies, and about 40% high at high energies, presumably dominated by inaccuracies in the Monte Carlo simulations.

The stability of the nuclear-recoil acceptance over time is checked by Fig. 28, which shows the rates of muon-coincident nuclear-recoil candidates, coadded over the three good detectors, as a function of time in blocks of approximately 5 live days. The rate of shared-electrode candidates is much higher for the data at 4-V ionization bias, which corresponds to the second and third bins in the plot. This evidence of likely contamination for the 4-V data, combined with further evidence of worse contamination in detector BLIP 3 and in the outer-electrode data during this time period, leads us to discard the 4-V shared-electrode data from the dark-matter analysis. The rates of the single-scatter (multiple-scatter) candidates are otherwise stable to 10% (20%), consistent with statistical fluctuations. In particular, the rates show no statistically significant change at either the

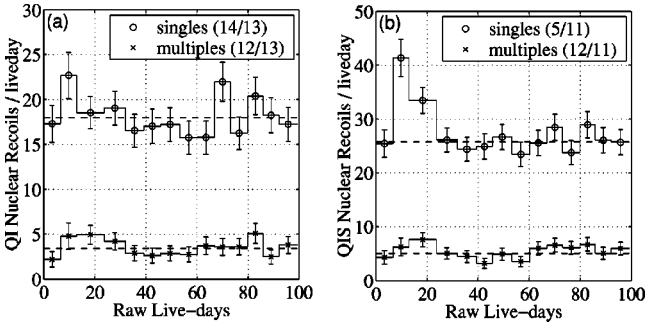

FIG. 28. Rates of muon-coincident single-scatter (upper data) and multiple-scatter (lower data) neutron candidates vs time, coadded over BLIPs 4–6, for recoil energies between 10–100 keV. Each bin corresponds to approximately 5 live days. Statistical uncertainties are shown as error bars. The χ^2 and degrees of freedom of the data relative to the mean (dashes) calculated from the data are shown as a fraction in the legend. (a) Events with at least one hit fully contained in the inner electrode. (b) Events with at least one hit with any energy in the inner electrode (QIS events). The increased number of veto-coincident shared-electrode events passing the nuclear-recoil cut during data taken with 4-V ionization bias (second and third bins) is consistent with other evidence leading to the discarding of the 4-V shared-electrode data set from dark-matter analysis.

April 3 power outage or the refrigerator warmup/cooldown cycle in June; these events occurred at roughly 29 and 65 raw live days, respectively.

Overall, the checks of the various cut efficiencies suggest that the efficiencies are accurate and stable at about the 10% level. Such accuracy is more than sufficient because the statistical uncertainties are considerably larger.

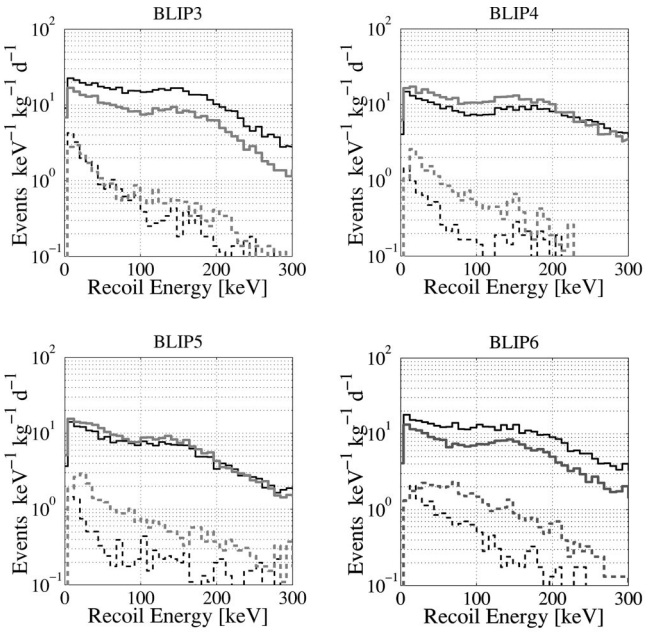

FIG. 29. Recoil-energy spectra for veto-coincident inner-electrode contained events. Dark solid line: single-scatter photons. Dark dashed line: single-scatter electrons. Light solid line: photons belonging to double scatters. Light dashed line: electrons belonging to double scatters.

D. Low-background data

At the experiment's current shallow site, most events are induced by muons and tagged by the muon veto. The observed electromagnetic backgrounds coincident and anticoincident with the veto are $60\ \mathrm{keV}^{-1}\,\mathrm{kg}^{-1}\,\mathrm{d}^{-1}$ and $2\ \mathrm{keV}^{-1}\,\mathrm{kg}^{-1}\,\mathrm{d}^{-1}$. Recoil-energy spectra for the veto-coincident data are shown in Figs. 29 and 30. Events with ionization yields consistent with bulk electron recoils are histogrammed as photons, while events with ionization yields inconsistent with bulk electron recoils and nuclear recoils are histogrammed as electrons. The relative single- and double-scatter rates reflect the geometry; BLIPs 3 and 6, the detectors on the top and bottom of the stack, exhibit lower double-scatter photon fractions than BLIPs 4 and 5, the detectors with two nearest neighbors. Also, compared to the veto-anticoincident data, the electron double-scatter fractions are quite high, indicating most veto-coincident electrons are produced in showers or are ejected from the detectors and surroundings. The photon spectrum incident on the detectors is expected to decrease with decreasing energy at low energy due to the presence of many shielding layers. The shared-electrode events reflect the incident spectrum because internal multiple scatters are included in this set, increasing the number of events with the full photon energy deposited in the detector. In contrast, the spectrum of inner-electrode-contained photons increases with decreasing energy at low energy, as expected from the fact that such events are dominated by Compton scattering of high-energy photons.

The dominant muon-anticoincident electromagnetic background is due to natural radioactivity, long-lived cosmogenic activation, or possibly thermal-neutron activation. For the data set described here, the veto efficiency for muons that pass through the detectors was $>99.9\%$. The muon-induced veto-anticoincident event rate is therefore $<0.1\ \mathrm{keV}^{-1}\,\mathrm{kg}^{-1}\,\mathrm{d}^{-1}$, far less than the observed total anticoincident rate of $\sim 1\ \mathrm{keV}^{-1}\,\mathrm{kg}^{-1}\,\mathrm{d}^{-1}$ (see Figs. 31 and 32). Attempts to simulate this radioactivity-induced background level, assuming reasonable amounts of radioisotopes in the construction materials, have thus far failed to yield a rate as high as that observed. Because the energy of $\sim$ MeV photons is rarely fully contained in these low-mass detectors, high-energy spectral lines that could otherwise be used to determine the abundance of particular radioactive contaminants are not visible, as shown in Fig. 33.

The rate of α particles interacting in the detectors is about 0.8 per live day per detector, and about 0.2 per live day in the fiducial volume of each detector. No evidence of α decays in the bulk of the detectors is seen, consistent with expectations based on the purity of the materials. Because α particles result in high-energy depositions, well above the energy region of a potential WIMP signal, they do not provide a significant background for the WIMP search. The recoiling nuclei from α decays may result in low-energy events. We have tagged several such events by each one's coincidence with an α particle in an adjacent detector. Because the recoiling nu-

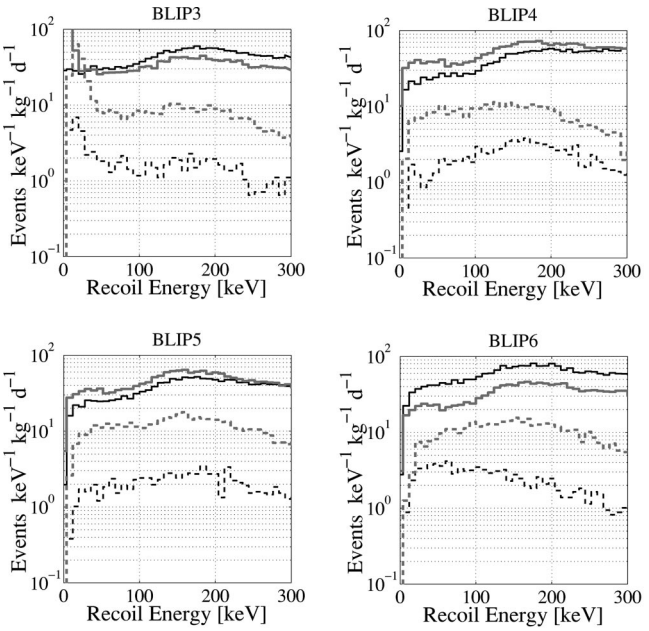

FIG. 30. Recoil-energy spectra for veto-coincident shared-electrode events. The legend is as in Fig. 29.

clei interact in the detector's dead layer, they result in little or no ionization and hence yield events outside the nuclear-recoil acceptance region.

1. Muon-anticoincident nuclear recoils

Figure 34 shows plots of ionization yield vs recoil energy for the muon-anticoincident events triggering on any single detector (the WIMP multiple-scatter rate is negligible). Bulk electron recoils (primarily due to photon interactions) lie at ionization yield $Y \simeq 1$. Low-energy electron events form a distinct band at $Y \sim 0.75$, leaking into the nuclear-recoil acceptance region below 10 keV. Between 10 and 100 keV, 23 QIS (13 QI) unvetoed nuclear-recoil candidates are observed, corresponding to 15.8 (11.9) kg d exposure. Figure 35 displays the recoil-energy spectrum of unvetoed single-scatter nuclear-recoil candidates for the Ge data set, along with the overall efficiency.

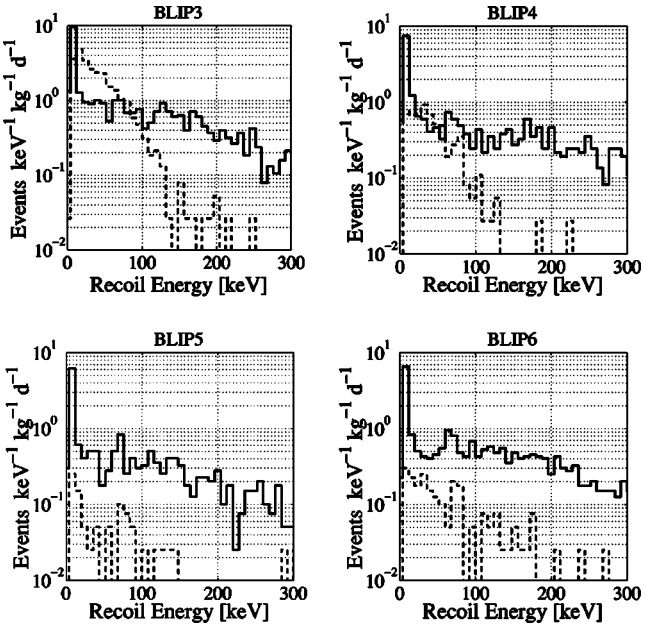

FIG. 31. Single-scatter photon and electron recoil-energy spectra for veto-anticoincident inner-electrode-contained events. Solid line: photons. Dashed line: electrons.

2. Expected nuclear-recoil-band contamination

The observed photon and electron event rates can be combined with the photon- and electron-calibration data to set upper limits on the expected numbers of misidentified single-scatter photons and electrons in the low-background set. As shown in Table II, photon misidentification should contribute a negligible number of nuclear-recoil candidates. The estimate on the amount of electron misidentification is not nearly so useful, for two reasons. First, the electron calibration is statistics-limited: even if no nuclear-recoil candidates had been seen in the electron calibration, the 90% C.L. upper limits would still be non-negligible. Second, the two electron-calibration events with both hits in the nuclear-recoil acceptance region (see Fig. 36) may well be multiple-scatter neutrons (about one multiple-scatter neutron is expected in this data set). However, to be conservative, Table II lists these events as misidentified electrons. With this conservative assumption and low statistics, it is possible for all of the low-background nuclear-recoil-candidate events to be misidentified electrons. However, the most likely number of misidentified electrons, even with this conservative assumption, is only about 6 QIS (3.6 QI) events. Most of the single-scatter nuclear-recoil candidates are probably nuclear-recoil events.

3. Consistency tests

The self-consistency of the hypothesis that the nuclear-recoil candidates are all veto-anticoincident nuclear recoils is tested by comparing the distributions of various event parameters to their expected distributions using the Kolmogorov-Smirnov (KS) test (see [53] or [56]).

Figure 37 shows the cumulative distribution of the last veto-trigger times for the 20 QIS (10 QI) ionization-trigger nuclear-recoil candidates (three of the nuclear-recoil candidates are phonon-trigger events). These times should follow an exponential distribution if the veto-trigger times are uncorrelated with the event times. The KS test indicates that 42% (55%) of experiments should observe distributions that deviate further from the expected exponential distribution for the QIS (QI) events.

It is also possible to test the time distribution of the events. The integrated exposure, the number of kg days of data taken up to the time of an event, takes into account the cut efficiencies and the numbers of detectors that were live for each event. Any unvetoable set of events (such as those due to WIMPs) should be uniformly distributed in exposure. For events caused by cosmic-ray muons that avoid being vetoed due to the small residual veto inefficiency, the time dependence of the veto efficiency must be included in the calculation of the expected fraction of events observed as a

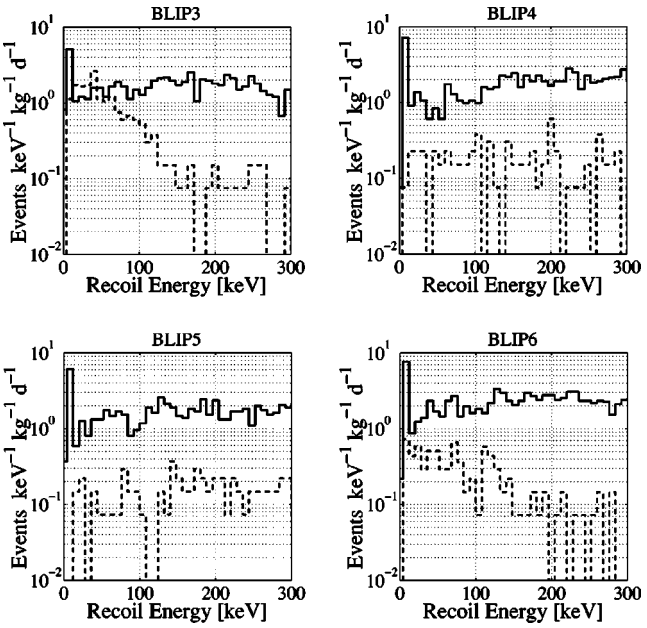

FIG. 32. Single-scatter photon and electron recoil-energy spectra for veto-anticoincident shared-electrode events. Solid line: photons. Dashed line: electrons.

function of the cumulative exposure. For events caused by particles much less likely to be vetoed (such as neutrons produced outside the veto), the time dependence of the veto efficiency is likely negligible. The KS test indicates 51% (60%) of experiments should observe distributions that deviate further from the distribution expected for QIS (QI) events for a constant veto efficiency. For QIS (QI) events whose veto probability is directly proportional to the veto probability for muons, the KS test indicates that 30% (82%) of experiments should observe distributions that deviate further from the expected distribution. The time distribution of the events agrees with expectations under each of these hypotheses.

The distribution in ionization yield of the nuclear recoils can be compared to the expected distribution. The normalized deviation, Y^*, is defined by

$$Y^* \equiv \frac{Y - Y_{\mathrm{NR}}(E_{\mathrm{R}})}{\sigma_{\mathrm{NR}}(E_{\mathrm{R}})}, \tag{10}$$

where $Y_{\mathrm{NR}}(E_{\mathrm{R}})$ is the expected ionization yield of a nuclear recoil and $\sigma_{\mathrm{NR}}(E_{\mathrm{R}})$ is the standard deviation of Y for nuclear recoils, both functions of E_{R}. The usefulness of Y^* is that it puts nuclear recoils at different E_{R} on the same footing. In the absence of cuts in Y defining the acceptance region, the expected distribution is a simple Gaussian with mean $\mu = 0$ and standard deviation $\sigma = 1$. The ionization-threshold cut that defines the nuclear-recoil band truncates the distribution in an E_{R}-dependent manner that is calculated for each of the 23 QIS (13 QI) single-scatter nuclear recoils. Figure 37(c) shows the expected and actual distributions. The KS test indicates that 76% (77%) of experiments should observe distributions that deviate further from the expected distribution. This level of agreement is important because misidentified electron events would be expected to have a distribution either flat in Y or weighted toward high Y.

The single-scatter nuclear-recoil candidate events are consistent in every way with being nuclear recoils, and the expected contamination from misidentification is only a few events, even under the conservative assumption that there are

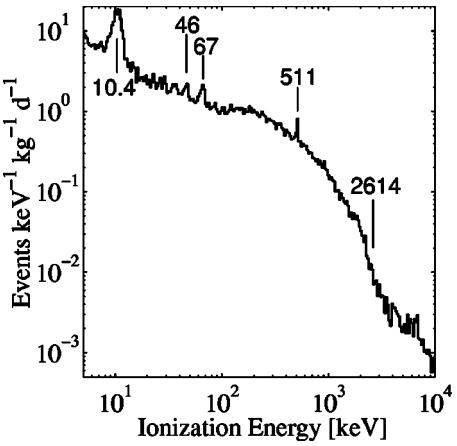

FIG. 33. Spectra for veto-anticoincident events with no other cuts applied, showing the sum of the ionization electron-equivalent energy in all four detectors. Bin widths are logarithmic and roughly correspond to the energy resolution at high energies. Significant spectral lines at 10.4 keV (from internal Ga), at 67 keV (from ^{73m}Ge), and at 511 keV (from positron annihilation) are indicated. The line at 46 keV (from ^{210}Pb) is significant only when a cut selecting events in the outer electrode is applied. See also Fig. 13. The rate of events above the 2.6 MeV end point of U/Th is much lower than the rate below this energy, suggesting that a significant fraction of the lower-energy events are due to U/Th contamination.

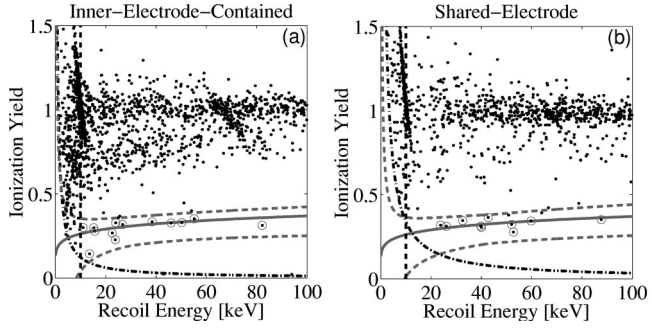

FIG. 34. Ionization yield (Y) vs recoil energy for veto-anticoincident single scatters in the 3 uncontaminated Ge detectors. Solid curve: expected position of nuclear recoils. Dashed curves: mean nominal 90% nuclear-recoil acceptance region. Dashed line: 10 keV analysis threshold. Dotted-dashed curve: mean threshold for separation of ionization signal from amplifier noise. Circled points: nuclear recoils. (a) Events with energy fully contained in the detectors' inner electrodes. (b) Events with energy shared between the detectors' inner and outer electrodes. The presence of 2 uncircled events within the mean nuclear-recoil band is due to slight differences in the size of the band for different detectors. About half the 3 QI (4 QS) events just above the acceptance region are likely to be nuclear recoils, since the top of the nuclear-recoil band is 1.28σ above its center, yielding 90% acceptance.

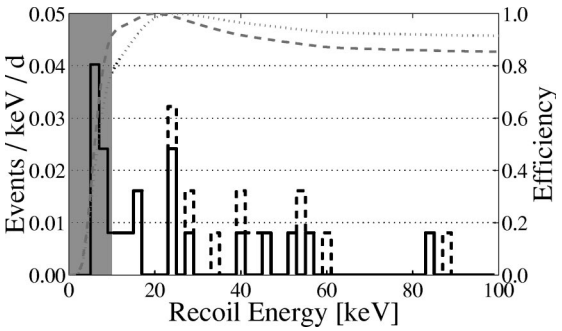

FIG. 35. Histogram of inner-electrode-contained (solid) and shared-electrode (dashed) veto-anticoincident single-scatter nuclear recoils observed in the 3 uncontaminated Ge detectors (left-hand scale). The nuclear-recoil efficiencies (right-hand scale) for the QI (dashed) and QIS (dotted) data are each peak normalized to 1; with this normalization, the QIS data corresponds to 0.26 kg effective mass, and the QI data corresponds to 0.20 kg effective mass. Shaded: 10 keV analysis threshold.

no neutrons in the electron-calibration data set. It therefore appears that the nuclear-recoil candidates are mostly, if not entirely, actual nuclear-recoil events. In order to set a conservative upper limit on the number of WIMPs in the data set, we will assume that all these nuclear-recoil candidates are nuclear-recoil events.

V. ESTIMATE OF NEUTRON BACKGROUND

As described in Sec. II E, a significant unvetoed neutron background is expected due to neutrons produced outside the muon veto by high-energy photonuclear and hadronic shower processes induced by cosmic-ray muons. The expected production spectrum

$$dN(E) \propto \begin{cases} 6.05\ \exp(-E/77\ \text{MeV})\ dE, & E < 200\ \text{MeV}, \\ \exp(-E/250\ \text{MeV})\ dE, & E > 200\ \text{MeV}, \end{cases} \tag{11}$$

is shown in the top graph of Fig. 38. The spectrum is based on a compilation of measurements shown in Fig. 4 of [51], whose authors note that ''the spectra do not depend on the projectile (π, p, n, γ) and its energy provided the latter is greater than 2 GeV.'' Hence, this single two-component spectrum is used for the high-energy photonuclear and hadronic shower processes. The production rate of 4 $\text{kg}^{-1}\,\text{d}^{-1}$, which would yield an integral flux of these neutrons into the tunnel of 2×10^{-6} $\text{cm}^{-2}\,\text{s}^{-1}$, is quite uncertain; the true production rate and flux could be as much as two times larger or smaller. Monte Carlo simulations of the CDMS experiment indicate that $\sim$40% of these externally produced neutrons are tagged as muon coincident due to their interactions in the veto scintillators. However, additional uncertainty arises because an unknown fraction of the hadronic showers associated with neutron production may also trigger the veto. Furthermore, the energy spectrum may differ somewhat from that given in Eq. (11) due to contributions from projectiles with energies <2 GeV/c^{-2}. Due to these uncertainties in both the rate and the energy spectrum, no quantities that depend significantly on the neutron production spectrum should be considered reliable for neutron background estimation.

TABLE II. Veto-anticoincident inner-electrode and shared-electrode single-scatter photon and electron misidentification estimates. The first two columns list the numbers of properly identified calibration events N_c and calibration events misidentified as nuclear recoils N_l in BLIPs 4–6 (BLIPs 3–4) for the photon-calibration (electron-calibration) data sets. The third column lists the number of single-scatter background events N_b in the given data set and energy range. The final two columns list the resulting expected number of events misidentified as nuclear recoils $\langle \mu_l \rangle$ as well as the Bayesian 90% C.L. upper limit $\mu_{l,90}$ on this quantity. The expected misidentification for the full energy range need not be equal to the sum of the expected misidentification for the two smaller energy ranges.

Event set	N_c	N_l	N_b	$\langle \mu_l \rangle$	$\mu_{l,90}$
Inner-electrode-contained photons					
10–30 keV	4661	2	490	0.2	0.6
30–100 keV	5609	0	498	0.0	0.2
10–100 keV	10270	2	988	0.2	0.5
Shared-electrode photons					
10–30 keV	2430	0	172	0.0	0.2
30–100 keV	4466	1	508	0.1	0.4
10–100 keV	6896	1	680	0.1	0.4
Inner-electrode-contained electrons					
10–30 keV	95	2	101	2.1	5.9
30–100 keV	61	0	180	0.0	7.0
10–100 keV	156	2	281	3.6	9.7
Shared-electrode electrons					
10–30 keV	23	1	31	1.3	5.8
30–100 keV	20	0	78	0.0	9.7
10–100 keV	43	1	109	2.5	10.3

Fortunately, the low-energy spectrum of neutrons incident on the detectors due to these high-energy external neutrons does not depend significantly on the details of the production spectrum. The low-energy part of the incident spectrum, made up of secondary and tertiary neutrons, is evaporative, just like the spectrum of low-energy neutrons resulting from negative muon capture [57]. For this reason, the incident spectrum due to external neutrons (shown in Fig. 38) is essentially the same at low energies (<5 MeV) as that due to the veto-coincident, ''internal'' neutrons which, as explained in Sec. II E, arise from negative muon capture and low-energy photonuclear interactions of muons within the shield. While the internal neutron spectrum is taken from the literature [33,58], the incident spectrum due to high-energy external neutrons is obtained by simulating the propagation and showering of these neutrons within the shield. Good agreement at low energy between the two spectra indicates that secondary production is well simulated. Studies of simulations confirm that the spectrum of secondaries at the detec-

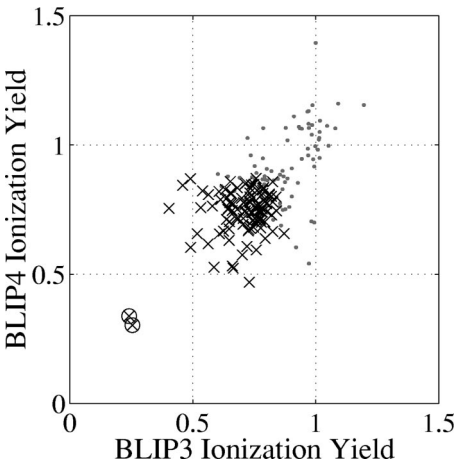

FIG. 36. BLIP 4 ionization yield vs BLIP 3 ionization yield for events ($\times$'s) used as the electron-calibration data set. This set consists of all veto-anticoincident double-scatter events in BLIP 3 and BLIP 4 with both hits between 10–100 keV, at least one QIS hit, and no hit that appears as a bulk electron recoil ($Y \sim 1$). Events with one or more apparent bulk electron recoils that fulfill all other criteria are shown as dots. Two events (circled) pass nuclear-recoil cuts for both BLIP 3 and BLIP 4. Based on the expected neutron background, about one double-scatter neutron should be in this data set. The large separation from the main distribution of the two events tagged as nuclear recoils in both BLIP 3 and BLIP 4 suggests they are, in fact, neutrons; in the analysis, they are conservatively assumed to be misidentified electrons.

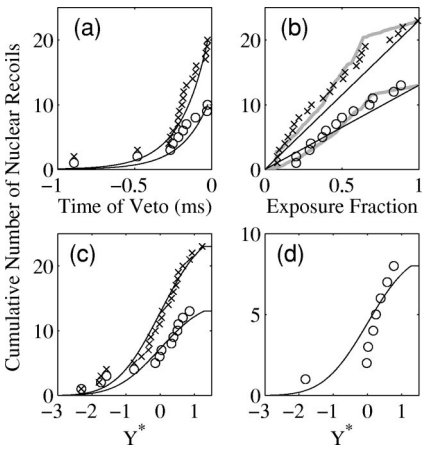

FIG. 37. Comparisons of expected integral distributions (curves) to actual integral distributions for veto-anticoincident QIS ($\times$'s) and QI (circles) nuclear-recoil candidates. (a) The last veto-trigger time for ionization triggers. (b) Exposure fraction. The dark lines show the expectations if the rate of events should be uncorrelated with changes in veto efficiency with time, while the gray curves indicate the expectations if the rate of events should be linearly correlated with changes in the veto efficiency. (c) Single-scatter Y^* distributions. (d) Multiple-scatter Y^* distributions. As quantified in the text, all distributions are consistent with expectations.

tors is largely insensitive to features in the primary spectrum [55]. The spectral shape of primaries affects only the absolute rate and the high-energy tail ($\gtrsim 5$ MeV) of the incident energy spectrum of the secondary neutrons.

The detector recoil-energy spectra in the range of interest (<100 keV) are dominated by interactions with low-energy neutrons ($\lesssim 5$ MeV) due to simple kinematics and the suppression of neutron cross sections at high energy. Therefore, the expected recoil-energy spectra below 100 keV due to external and internal neutrons are almost identical in shape, as shown in Fig. 38. The predicted spectral shape of all neutron interactions is therefore insensitive to the relative numbers of interactions arising from neutrons that originate internally versus externally. Other normalization-independent predictions include the fraction of neutrons that scatter in multiple detectors, and the relative rates of neutron interactions in Ge and Si. These results are also nearly independent of the primary neutron spectrum and are almost the same for internal and external neutrons. Only these normalization-independent quantities are used to estimate the neutron background in the low-background data.

Comparison of Monte Carlo results with the calibration and internally produced neutron data sets provides checks of the accuracy of the neutron simulations, particularly for these normalization-independent quantities, as well as checks of the efficiency calculations described in Sec. IV C 10. As discussed in Sec. IV C 9, calculation of the efficiency for multiple-scatter events is nontrivial due to correlations in the cuts for detector combinations. Estimates of the systematic uncertainty of these efficiency calculations combine to give an overall systematic uncertainty of 8% on the expected measured fraction of neutron interactions that are identified as multiple scatters. These uncertainties are due primarily to the 10% uncertainty on the fiducial-volume efficiency at low energies (which results in a 5% uncertainty on the expected fraction of neutrons identified as multiple scatters), and a possible 5% uncertainty on the correlated efficiencies discussed in Sec. IV C 9.

Studies of the Monte Carlo simulation, including comparisons to standard cross sections and to results from GEANT4 simulations, indicate that inaccuracies in the Monte Carlo simulation should not cause an error on the predicted neutron multiple-scatter fraction larger than 10%. In particular, a negligible error should result from the fact that the simulation ignores the possibility that an external neutron may be accompanied by other external neutrons from the same shower. Using an approximate muon energy spectrum [59] and muon ionization loss [60], along with results of a calculation of neutron yield and multiplicity distribution per muon [61], we find that a neutron generated at SUF depth by a muon with energy >10 GeV is accompanied on average by only 10 other neutrons in the same shower. This average is not very sensitive to the low-energy cutoff in muon energy. Because our Monte Carlo simulation shows that external neutrons reaching the experimental shielding have only a 10^{-4} probability of hitting a detector, the neutron production multiplicity has a negligible effect on the probability of detecting multiple scatters. Furthermore, a simple calculation assuming an isotropic neutron flux, isotropic elastic scattering, and an appropriate interaction cross section, verifies the multiple-scatter fractions predicted by the Monte Carlo simulation for the simple case of the neutron calibration. Combining the uncertainty on the efficiencies with the possible

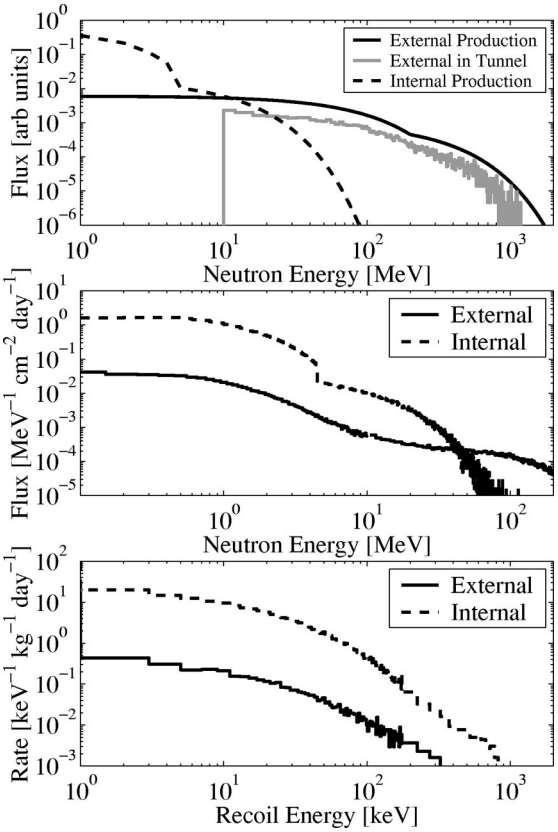

FIG. 38. Top: Arbitrarily normalized expected production spectra of internal (dashed curve) and external (solid curve) neutrons. The resulting simulated spectrum of external neutrons after propagating through the tunnel rock (gray solid curve) is cut-off artificially at 10 MeV. Neutrons below this energy are unimportant because a negligible number of lower-energy neutrons penetrate the experiment's shielding. Middle: Expected spectra of internal and external neutrons incident on the detectors. Below about 4 MeV, the two spectral shapes match closely. Bottom: Resulting simulated recoil-energy spectra in Ge for both internal and external neutrons. Note that an incident neutron can impart at most 1/18 of its energy to Ge in a single elastic scatter. Despite the extremely different production spectra of the primary neutrons, the recoil-energy spectra below 100 keV are nearly identical, as explained in the text.

systematic error of the Monte Carlo simulation results in an overall systematic uncertainty on this fraction of 13%.

Based on the neutron simulations, Table III shows the expected neutron-background rates. The simulated and observed multiple-scatter-neutron spectra are shown in Fig. 39. All recoils of a multiple-scatter event are required to be between 10 and 100 keV for the event to pass cuts. Each histogram is filled for each recoil of a multiple-scatter event; e.g., a double scatter adds two entries to the histogram. For the neutron calibrations, the simulation predicts a 20% higher overall rate than is observed, along with a slightly harder energy spectrum than is observed. For the veto-coincident neutrons, comparisons are hampered by the fact that the fraction of neutrons coincident with other muon-induced particles is unknown. Accurate measurement of the rate of these coincidences is complicated by the fact that interactions of several MeV in one detector produce crosstalk of $\sim$10 keV in neighboring detectors, potentially making electron-recoil events indistinguishable from neutron-induced events. These problems, combined with the fact that the production of the muon-induced particles other than neutrons is not as yet simulated, results in a 20% systematic uncertainty on the measured rate of veto-coincident neutrons, and a 20% systematic uncertainty on the measured fraction of neutrons that multiply scatter.

Table IV lists the overall scale factors by which the simulated spectra must be scaled to match the data. Comparisons of the ratios of single-scatter events to multiple-scatter events for the calibration and internally produced neutrons provide checks of the accuracy of the prediction of the same ratio for veto-anticoincident neutrons. For each data set, the ratios agree with those predicted to within the combined systematic and statistical uncertainties. The good agreement between data and the results of the Monte Carlo simulations builds confidence in the predictive power of using normalization-independent results of the Monte Carlo simulation for estimating the external neutron background. The predicted ratios of the different classes of neutron events, together with the observed number of Ge multiple-scatter neutrons and the number of neutron events in the Si detector, should provide a dependable estimate of the expected number of neutron single scatters in the Ge data set.

A. Ge multiple-scatter data set

Figure 40 displays a scatter plot of ionization yields in one detector versus those in another for low-background multiple scatters. The four Ge multiple-scatter nuclear-recoil candidates should all be multiple-scatter neutrons. WIMPs interact too weakly to multiply scatter. It is also highly unlikely that these events are misidentified low-energy electron events. Figures 34 and 40 demonstrate excellent separation of low-energy electron events from nuclear recoils. As shown in Fig. 37(d), the multiple-scatter nuclear-recoil candidates have Y^* values consistent with those expected for nuclear recoils (a KS test indicates 9% of experiments should result in a distribution less similar to expectations). Finally, three of the events have both hits with energy in the inner electrode, consistent with expectations for neutrons. If these events were due to misidentification of electron-induced events, more hits would likely be in the outer electrode since misidentification occurs much more often for hits in the outer electrode, as shown in Fig. 24.

The expected number of misidentified multiple-scatter electron recoils may be estimated quantitatively. As described above, BLIP 3 and BLIP 4 multiple scatters with too little ionization in both BLIP 3 and BLIP 4 to be photons may be used as a low-statistics electron calibration. Of the 216 hits tagged as electrons (or neutrons) in BLIP 3 or BLIP 4, only 4 pass the nuclear-recoil cut, so the expected fraction of electron misidentification $\beta_\beta = 4/216$ under the conservative assumption that none of the hits are neutrons. In using the electron calibration to estimate the number of double-scatter nuclear-recoil candidates arising from misidentified electrons, it is important to make use of the fact that, while the double-scatter electrons do cluster around $Y \sim 0.75$, there

TABLE III. Expected rates of neutron interactions per kg day between 10–100 keV (20–100 keV) for Ge (Si) detectors at SUF. The numbers in parentheses indicate the rates expected for ideal detectors with energy-independent efficiency, no dead periods, and both hits of a multiple scatter required to be in the fiducial volume (the last requirement causes the rate of multiple-scatters to be smaller for these ''ideal'' detectors than for the actual detectors). As discussed in the text, the expected rate of external neutrons is quite uncertain. The rate of internal neutrons is much better determined, with systematic uncertainties ~10%. Only the prediction for neutrons from the outer lead has a significant statistical uncertainty (~25%). Because the mass of the inner lead shield was increased between the 1998 Si data run and the 1999 Ge data run, the fraction of interactions due to neutrons produced in the inner lead is slightly greater for the Ge detectors than for the Si detector.

Source	Ge singles	Ge multiples	Si singles
		Internal	
Copper	72 (76)	8 (6)	142 (177)
1998 inner lead			125 (155)
1999 inner lead	75 (79)	8 (6)	
Outer lead	~6 (6)	~0.8 (0.6)	~11 (14)
Total	153 (161)	17 (13)	278 (346)
		External	
Rock	3.0 (3.2)	0.3 (0.2)	5.0 (6.3)

is no correlation between the two detectors' deviations from this central value of the ionization yields, as seen in Fig. 36—the electron events do not form a line with slope 1. In order to be misidentified as a double-scatter neutron, a double-scatter electron must therefore be misidentified in *both* detectors; such misidentification is suppressed by a factor β_β^2 rather than only β_β.

The lack of correlation between the ionization yields in the two detectors is expected because energy deposited in the first detector is not a strong function of the electron energy—it depends on the track length in the crystal, which may be short for a high-energy electron if it is backscattered. The ionization yield is, however, well correlated with the track length: shorter tracks are also likely to be more shallow. Thus, for double-scatter electrons, the ionization yield for one scatter, while correlated with the deposited energy, may not be a good predictor of the actual electron energy, and thus may not be a good predictor of the ionization yield observed in the second recoil.

As shown in Fig. 40, most veto-anticoincident double scatters between BLIPs 4, 5 and 6 appear to be photons, with ionization yield $Y \sim 1$ for both hits. Note that most multiple-scatter photon events do not appear on this plot, either because energy is deposited in three or more detectors, or because at least one energy deposition is outside the 10–100 keV energy range. Monte Carlo simulations of generic sources of radioactive contamination, such as U/Th in the detector housing, suggest that for every single scatter resulting in a recoil between 10–100 keV, there are ~0.07 double scatters with both recoils between 10–100 keV, and there are an additional ~0.6 multiple-scatter events. The fraction of

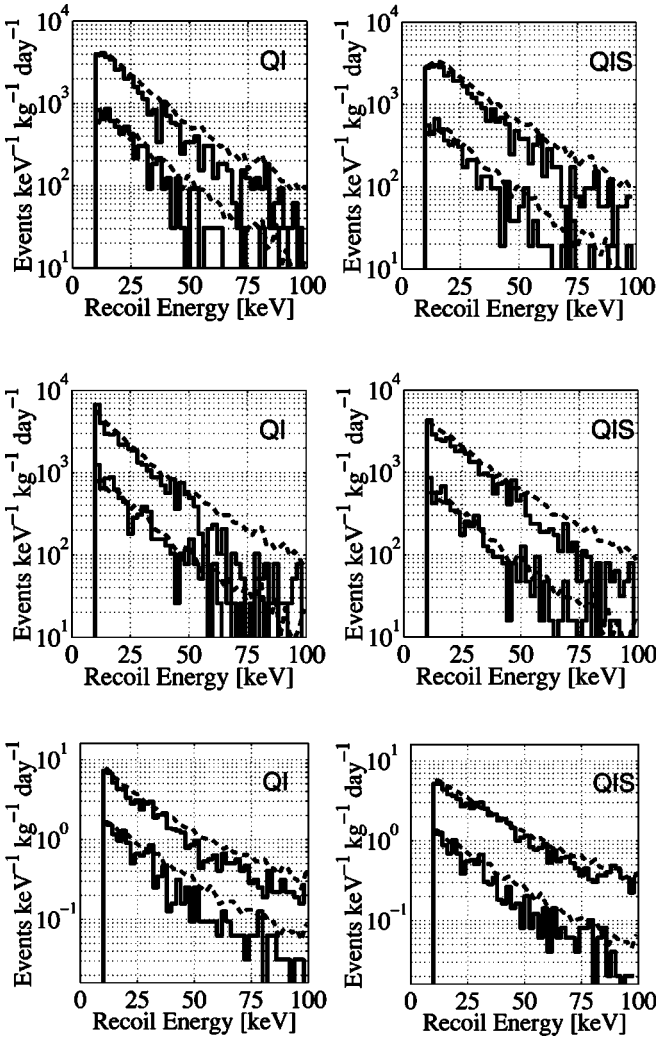

FIG. 39. Observed and simulated neutron-calibration and veto-coincident spectra, coadded over detectors, with no free parameters. In each plot, spectra both for all scatters (top) and for multiple scatters (bottom) are shown for both data (solid) and simulations (dashes). Figures in the left column show events with at least one QI scatter; figures in the right column show events with at least one QIS scatter. Top: first neutron calibration. Middle: second neutron calibration. Bottom: veto-coincident (internal) neutrons. The calibration data are coadded over all four detectors; the veto-coincident data is coadded over BLIPs 4–6.

photon events that appear as double scatters appears consistent with expectations from these simulations if one takes into account the large number of 10.4 keV photons unlikely to multiple scatter.

There are also 16 events with both hits having ionization yield Y lower than typical photons, and an additional 21 events with one of the two hits having lower Y than typical photons. To be conservative, we count the total number of $16\times 2+21=53$ low-Y hits as yielding an effective $N_\beta=26.5$ double-scatter surface-electron events. The expected number of misidentified surface-electron-recoil double-scatter events is therefore only $N_\beta\beta_\beta^2=26.5\times(4/216)^2=0.009$. The upper limit at the 90% confidence level on the number of double-scatter electrons expected to

TABLE IV. Scaling factors that must be applied to the results of the simulation to match the total rates observed in BLIPs 4–6. Data sets include both QIS and QI nuclear recoils (NRs), and multiple scatters with at least one QI scatter (''multiple QI NRs'') and those with at least one QIS scatter (''multiple QIS NRs''). Statistical uncertainties are 6–7 % for multiple scatters and 2–3 % for all events. As can be seen, the overall rates predicted are accurate to ~20%, and the predicted fractions of events that are multiple scatters are accurate to ~10%.

Event set	First neutron calibration	Second neutron calibration	Veto-coincident neutrons
All QI NRs	0.82	0.80	0.81
Multiple QI NRs	0.86	0.93	0.73
All QIS NRs	0.79	0.77	0.88
Multiple QIS NRs	0.86	0.91	0.77

be misidentified as double-scatter neutrons is $b_d = 0.05$ events. Even if the misidentification were somehow correlated between the two detectors, the expected number of misidentified electron-recoil hits would be only $N_\beta \beta_\beta = 26.5 \times (4/216) = 0.5$, again under the conservative assumption that neither of the calibration-set nuclear-recoil candidates are neutrons. Misidentified electrons provide truly negligible contamination of the four neutron multiple-scatter events. The Ge multiple-scatter data therefore provides a reliable estimate of the neutron background.

B. Si data set

An earlier run consisting of 33 live days taken with a 100 g Si ZIP detector between April and July 1998, also measured the neutron background. The Si run yields a 1.5 kg d exposure after cuts. The total low-energy electron surface-event rate is 60 $\mathrm{kg}^{-1}\,\mathrm{d}^{-1}$ between 20 and 100 keV. As shown in Fig. 41, four nuclear-recoil candidates are observed in the Si data set. Detailed analysis of this data is described elsewhere [24,25].

The four nuclear-recoil candidates observed in the 1998 Si ZIP data cannot be WIMPs: whether their interactions with target nuclei are dominated by spin-independent or spin-dependent couplings, WIMPs yielding the observed Si nuclear-recoil rate would cause far more nuclear recoils in the Ge data set than were observed. The WIMP-nucleus cross-section scales as A^2 for WIMPs with spin-independent interactions. Expected recoil-energy spectra in Ge and Si for a WIMP with spin-independent interactions are shown in Fig. 42. Ge and Si differ by a factor of 5 to 7 in differential rate between 0 and 100 keV. After including the effects of energy thresholds and efficiencies, one expects of order 90 (70) times the number of WIMPs in the 15.8 kg d QIS (11.9 kg d QI) Ge data set as in the 1.5 kg d Si data. The argument is more complicated for spin-dependent interactions, but it also holds that there should be many more nuclear recoils in the 1999 Ge data set than are observed. Furthermore, the spin-dependent cross section corresponding to the observed Si event rate is significantly larger than expected from the MSSM.

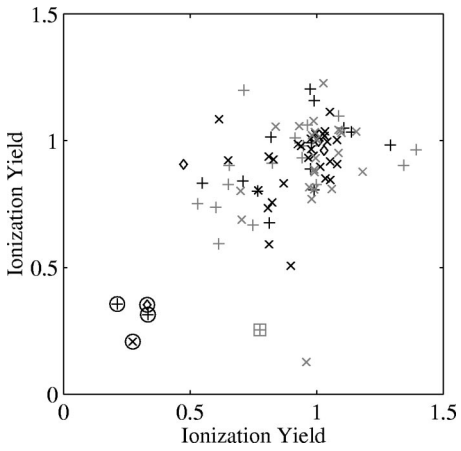

FIG. 40. Scatter plot of ionization yields for veto-anticoincident multiple scatters in the 3 uncontaminated Ge detectors with at least one QI (black) or QS (gray) scatter and with both scatters between 10 and 100 keV. Events are double-scatters in BLIP 4 and BLIP 5 [the top and middle uncontaminated detectors (+)], in BLIP 4 and BLIP 6 [the top and bottom uncontaminated detectors ($\diamond$)], or in BLIP 5 and BLIP 6 [the middle and bottom uncontaminated detectors ($\times$)]. The ionization yield of the higher-numbered detector is plotted on the *x* axis. Circled events are tagged as nuclear recoils in both detectors. The boxed event is tagged as a nuclear recoil in only BLIP 4. Bulk recoils and surface events lie at $Y \simeq 1$ and $Y \sim 0.75$, respectively. Both events with ionization yield $Y < 0.45$ in only one of the two detectors hit have the low-yield hit in the outer electrode, consistent with expectations for misidentification of electron recoils in the outer electrode.

It is possible, however, that not all of the Si nuclear-recoil candidates are neutrons. As shown in Fig. 41, the separation between the nuclear-recoil band and the electron-recoil band is not as large for the Si data as it is for the Ge data. A calibration of the Si detector with a ^{14}C electron source at a test facility provides a high-statistics estimate of the possible electron contamination. Based on the statistical uncertainties of this calibration, the upper limit on the expected number of unrejected surface events is 0.26 events (90% C.L.). However, the systematic uncertainties are larger, since this calibration was made with a collimated source and was taken under different conditions than the low-background data. A simple and conservative estimate of the contamination is made using data taken with a ^{60}Co photon source at SUF under essentially the same conditions as the low-background data. Assuming that all events passing nuclear-recoil cuts are due to the small number of electrons present in the calibration sample leads to an expectation of 2.2 low-background contamination events and an upper limit of 7.3 expected low-background contamination events at the 90% confidence level. For comparison, this assumption results in 13 (an upper limit of 17) events expected in the band just above the nuclear-recoil band below 30 keV, and 4.9 (an upper limit of 8.8) events expected in this band above 30 keV. As shown in Fig. 41, these predictions are in agreement with the 11 events in that band.

The measurement of the unvetoed neutron background from the 1998 Si data set is consistent with the measurement from the Ge multiple-scatter data set. However, the large systematic uncertainty on the Si data means the Ge data set dominates our combined measurement. We note that new Si and Ge ZIP detectors [62] perform significantly better than the Si ZIP of the earlier design used in 1998.

C. Neutron consistency tests

The fact that the observed number of single-scatter nuclear-recoil events in Ge is about as large as the expected background suggests that all such events may be due to neutrons. Although this possibility is of course not assumed in calculating limits on the WIMP-nucleon cross section, it is important to test the consistency of this possibility.

In fact, there is good agreement between predictions from the Monte Carlo simulation and the relative observed numbers of $N_{\rm d}=4$ QIS (4 QI) Ge double scatters, $N_{\rm Si}=4$ Si single scatters, and $N_{\rm s}=23$ QIS (13 QI) Ge single scatters. Schematically, the data and simulation can be compared in two ways: by normalizing the simulation by the neutron-background rate that best fits $N_{\rm s}$, $N_{\rm d}$, and $N_{\rm Si}$ jointly; or by normalizing by the neutron-background rate that best fits $N_{\rm d}$ and $N_{\rm Si}$ and predicting $N_{\rm s}$. The latter is the intuitive interpretation of using the Ge doubles and Si events to predict the neutron background in the Ge singles set. These comparisons are shown in Fig. 43.

More rigorously, a likelihood-ratio test can be used to compare the default hypothesis, that the $N_{\rm s}$, $N_{\rm d}$, and $N_{\rm Si}$ events are due to a neutron background with relative rates given by the simulation, to an alternate hypothesis, that the three event sets arise from three different background sources. Effectively, the latter hypothesis corresponds to three arbitrary background sources for the three event types, the most general possible hypothesis. This test indicates that a neutron background should result in a less likely combination of Ge QIS (QI) single scatters, Ge QIS (QI) multiple scatters, and Si single scatters $\gtrsim$48% (21%) of the time, with only weak dependence on the assumed true neutron background [34]. The self-consistency of the division of the neutrons into their five categories can also be tested. A neutron background should result in a less likely combination of Ge QS single scatters, Ge QI single scatters, Ge QS multiple scatters, Ge QI multiple scatters, and Si single scatters $\gtrsim$30% of the time.

Finally, as shown in Fig. 44, the observed nuclear-recoil spectral shape is consistent with expectations for neutrons whether the neutrons are produced internally or externally to the veto; recall that the expected internal and external neutron recoil-energy spectra should be similar because the recoil-energy spectrum is fairly independent of the high-energy tail of the external-neutron spectrum. Kolmogorov-Smirnov tests indicate that the deviation between the observed and simulated nuclear-recoil spectral shapes using the QIS (QI) events should be larger in 86% (39%) of experiments for external neutrons, and the deviation should be larger in 61% (67%) of experiments for internal neutrons. These results should be taken only as support for the consistency of the data with the neutron simulation; they do not alone disfavor an interpretation that some (or even all) events may be due to WIMPs. The spectra are also consistent with a combination of WIMPs and neutrons, or with WIMPs alone if the WIMP mass $M\gtrsim 100$ GeV/c^2.

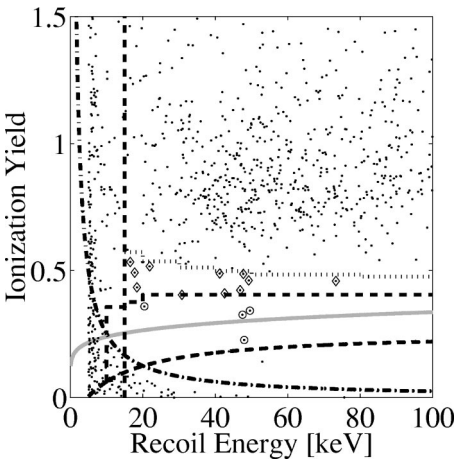

FIG. 41. 1998 Si ZIP detector veto-anticoincident data after cuts. Four nuclear-recoil candidate events (circled) lie near the center of the nuclear-recoil band (light solid curve), within the nuclear-recoil-acceptance region (bordered by dashed curves), and above both the ionization threshold (dotted-dashed curve) and nuclear-recoil analysis threshold (vertical dashed line). Eleven additional events (diamonds), of which $\sim$1 should be a nuclear recoil, lie in the band (bordered by the dotted curve) just above the nuclear-recoil band. These 11 events are consistent with the expected distribution of surface events based on *in situ* calibrations with photon sources. Events below the ionization threshold are likely dominated by events with poor charge collection in the outer ionization electrode. Events with recoil energies $E_{\rm R}<5$ keV are not shown.

VI. CALCULATING THE CONFIDENCE REGION

The 90% C.L. excluded region for the WIMP mass M and WIMP-nucleon cross section σ is derived using an extension of the approach of Feldman and Cousins [63]. The above

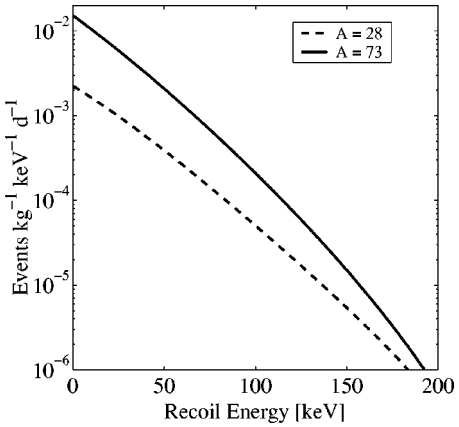

FIG. 42. Expected differential recoil-energy spectra for Si ($A=28$) and for Ge ($A=73$), for a 100-GeV/c^2 WIMP with WIMP-nucleon cross section $\sigma=10^{-42}$ cm^2 under standard assumptions listed in Sec. VI A.

arguments require accounting for the component of the N_s observed Ge single scatters (with energies E_i, $i=1,\ldots,N_s$) that is due to the unvetoed neutron flux n. This flux is constrained by the number N_d of double scatters in Ge and the number N_{Si} of nuclear recoils in Si. To determine the 90% C.L. excluded region in the plane of M and σ alone, the parameter n is projected out. For a grid of physically allowed values of M, σ, and n, the expected distribution of the likelihood ratio

$$R=\frac{\mathcal{L}(E_i,N_d,N_{Si}|\sigma,M,\tilde{n})}{\mathcal{L}(E_i,N_d,N_{Si}|\hat{\sigma},\hat{M},\hat{n})} \tag{12}$$

is calculated by Monte Carlo simulation in order to determine the critical parameter R_{90} such that 90% of the simulated experiments have $R>R_{90}$. Here $(\hat{\sigma},\hat{M},\hat{n})$ is the set of physically allowed parameters that maximizes the likelihood $\mathcal{L}$ for the given observations, while $\tilde{n}$ is the physically allowed value of n that maximizes the likelihood $\mathcal{L}$ for the given parameters M and σ and the observations. The 90% C.L. region excluded by the observed data set consists of all parameter space for which the observed likelihood ratio $R_{data}\leqslant R_{90}$. The 90% C.L. excluded region is projected into two dimensions conservatively by excluding only those points excluded for all possible values of n.

A. Likelihood function

The likelihood function consists of functions g describing the Poisson probabilities of obtaining the numbers of events actually detected, combined with a function f describing the probabilities of the events' energies:

$$\mathcal{L}=g_s(N_s|n,\sigma,M)g_d(N_d|n)g_{Si}(N_{Si}|n,\sigma,M)$$
$$\times\prod_i f_s(E_i|n,\sigma,M). \tag{13}$$

The energy spectrum of the multiple-scatter events is ignored because it cancels in the likelihood ratio. The energy spectrum of the Si events is also ignored, as it would influence the likelihood ratio very weakly.

The expected energy spectrum of detected WIMPs, $w_s(E)$, and their total number, w, are calculated by making standard (but probably over-simplifying) assumptions following [17]: WIMPs reside in an isothermal halo with WIMP characteristic velocity $v_0=220$ km s^{-1}, Galactic escape velocity $v_{esc}=650$ km s^{-1}, mean Earth velocity $v_E=232$ km s^{-1}, and local WIMP density $\rho=0.3$ GeV c^{-2} cm^{-3}. The energy spectrum of detected WIMP events also depends on the detection efficiency $\epsilon(E)$ and the nuclear form factor F^2. We use the Woods-Saxon (Helm) form factor F^2, with thickness parameters $a=0.52$ fm, $s=0.9$ fm, and $c=1.23A^{1/3}-0.6$ fm, as recommended by Lewin and Smith [17].

The resulting WIMP energy spectrum is well approximated by an exponential with a cutoff energy:

$$w_s(E)=\mathcal{N}e^{-E/\langle E\rangle}\epsilon(E)F^2(E)H(Q_{max}-E), \tag{14}$$

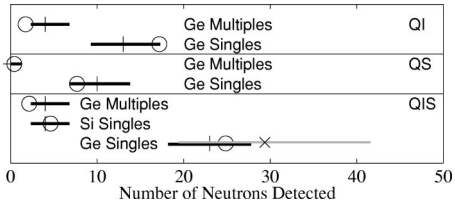

FIG. 43. Schematic comparison of predicted numbers of neutrons to observed numbers (crosses), with Feldman-Cousins 68% confidence level intervals [63] (dark lines). Predictions are made by normalizing the simulation by the neutron background that best fits N_s, N_d, and N_{Si} jointly (circles). An additional prediction for QIS Ge singles ($\times$, with the light line indicating the 68% confidence level interval) is based on the neutron background that best fits N_d and N_{Si} jointly. Top: inner-electrode-contained ("QI") events. Middle: shared-electrode ("QS") events. Bottom: events that are either contained in the inner electrode or shared between the electrodes ("QIS events"), together with Si events.

where $H(x)$ is the Heaviside step function (0 for $x<0$ and 1 for $x>0$), Q_{max} is the maximum possible recoil energy from a WIMP of velocity v_{esc}, $\mathcal{N}$ is a normalization constant, and $\langle E\rangle=E_0r/c_2$ in the notation of Lewin and Smith [17]. At low energies near the spectrum peak, this form differs $<5\%$ from Eq. (3.13) of Lewin and Smith. We use this approximation in order to speed up the calculation of the confidence region.

The neutron contribution to the energy spectrum, $n_s(E)$, is given by a best-fit function to the results of the external neutron Monte Carlo simulation including detection inefficiencies.

The Monte Carlo simulations, including the possible 13% systematic error on the fraction of neutrons that multiple scatter, set the expected fraction of single scatters $\beta_{QIS}=0.91$ ($\beta_{QI}=0.90$) amongst the Ge neutron events with at least one QIS (QI) scatter. Simulations also set the ratio $\gamma_{QIS}=0.17$ ($\gamma_{QI}=0.24$) of the number of neutrons expected in Si to the number expected in Ge with at least one QIS (QI) scatter. The expected ratio α of WIMPs detected in Si to those detected in Ge, given the relative exposures in each, depends weakly on the WIMP mass. For WIMPs with masses $M\gtrsim 30$ GeV/c^2 $\alpha_{QIS}\approx 0.011$ ($\alpha_{QI}\approx 0.015$). The expected electron background in Si b_{Si} is conservatively set to 7.3 events (corresponding to the 90% C.L. upper limit on the background expected in the 20–100 keV region under the

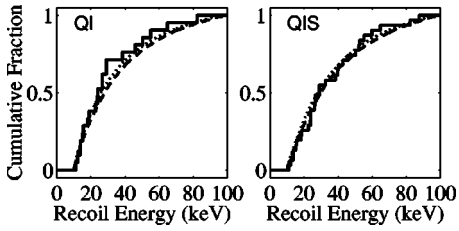

FIG. 44. Observed Ge nuclear-recoil integral recoil-energy spectra (solid), including single-scatter and multiple-scatter hits, for QI events (left) and QIS events (right). Observed spectra agree well with expectations from either the external-neutron (dashed curves) or the internal-neutron (dotted curves) simulations.

most conservative possible assumption). This treatment of the Si data is not correct (it is overly conservative). Ignoring the Si data, or using a better (and more complicated) treatment would result in a lower limit. We conservatively neglect possible electron contamination in the Ge single data. We also neglect the possibility of electron contamination in the multiple-scatter Ge data, since the analysis presented in Sec. V A indicates that the expected double-scatter contamination $b_{\rm d}<0.05$ at the 90% confidence level.

With these constants set, the expectation values for the observables are

$$\langle N_{\rm s}\rangle = n\beta + w, \tag{15}$$

$$\langle N_{\rm d}\rangle = n(1-\beta), \tag{16}$$

$$\langle N_{\rm Si}\rangle = n\gamma + w\alpha + b_{\rm Si}. \tag{17}$$

The pertinent contributions to the likelihood function are

$$g_{\rm k} = \frac{e^{-\langle N_{\rm k}\rangle}\langle N_{\rm k}\rangle^{N_{\rm k}}}{N_{\rm k}!} \tag{18}$$

for k $\equiv$ s, d, and Si, and

$$f_{\rm s}(E|n,\sigma,M) = \eta n_{\rm s}(E) + (1-\eta)w_{\rm s}(E), \tag{19}$$

where $\eta = n\beta/(n\beta + w)$ is the fraction of single-scatter Ge events expected to be neutrons. Dropping factors that cancel in ratios yields

$$\mathcal{L} \propto e^{[-n(1+\gamma)-w(1+\alpha)-b_{\rm Si}]} n^{N_{\rm d}} (n\gamma + w\alpha + b_{\rm Si})^{N_{\rm Si}} \times \prod_{i=1}^{N_{\rm s}} [n\beta n_{\rm s}(E_i) + w w_{\rm s}(E_i)]. \tag{20}$$

B. Calculating an upper limit assuming arbitrary background

Despite the evidence given above that the Ge single-scatter background is dominated by events due to neutrons, it is informative to calculate exclusion limits without using any information about the expected background. A near-optimal classical method, practical when there are relatively small numbers of events detected, is Yellin's ''optimum interval'' method [64]. Effectively, the method excludes the worst of the background by basing the limit on the interval in allowed energy that yields the lowest upper limit, while assessing the proper statistical penalty for the freedom to choose this optimum interval. The limit is essentially set by a region of the energy spectrum with few events compared to the number expected from the WIMP energy spectrum.

Every possible interval is considered, with intervals characterized by the numbers m of events in them, and $C_m(x,\mu)$ is defined as the probability that all intervals with $\leqslant m$ events have a computed expectation value of the number of events that is less than x, where μ is the expected number of events in the entire range of the measurement. For each value of m, the interval with the largest expected number of events x is determined. For intervals with no events, the probability of this maximum expected number being less than x is

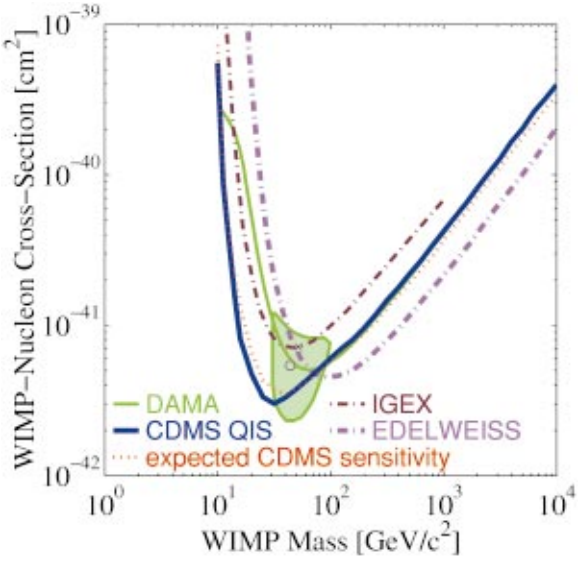

FIG. 45. (Color) Spin-independent σ vs M. The regions above the curves are excluded at 90% C.L. The limits resulting from an analysis of the QIS data (solid dark blue curve) are shown. The (red) dotted curve indicates the CDMS expected sensitivity given an expected neutron background of 27 events in Ge, and an expected background in Si of 7.2 electrons and 4.6 neutrons. Solid light (green) curve: DAMA limit using pulse-shape analysis [65]. The most likely value for the WIMP signal from the annual-modulation measurement reported by the DAMA Collaboration [66], calculated including (not including) the DAMA limit using pulse-shape analysis, is shown as a circle (as an x). The DAMA 3σ allowed region not including the DAMA limit [66] is shown as a shaded region. CDMS limits are the most sensitive upper limits for WIMPs with masses in the range 10–70 GeV/c^2. Above 70 GeV/c^2, the EDELWEISS experiment [67] provides more sensitive limits (dotted-dashed maroon curve). Also shown are limits from IGEX [68] (dotted-dashed brown curve). These and other results are available via an interactive web plotter [69]. All curves are normalized following [17] using the Helm spin-independent form factor, A^2 scaling, WIMP characteristic velocity $v_0 = 220$ km s^{-1}, mean Earth velocity $v_E = 232$ km s^{-1}, and $\rho = 0.3$ GeV/c^2 cm^{-3}.

$$C_0(x,\mu) = \sum_{k=0}^{m} \frac{(kx-\mu)^k e^{-kx}}{k!}\left(1 + \frac{k}{\mu - kx}\right), \tag{21}$$

where m is the greatest integer $\leqslant \mu/x$. For an interval with $m>0$ events, $C_m(x,\mu)$ is determined from Monte Carlo simulation.

$C_{\rm max}$ is defined as the maximum value of $C_m(x,\mu)$ for any m. A high assumed cross section leads to high $C_{\rm max}$ for this experiment's data; so if $C_{\rm max}$ is ''unreasonably'' high, the assumed cross section can be rejected as being too high. The expected probability distribution of $C_{\rm max}$, as determined with a Monte Carlo simulation, is used to compute a 90% confidence region.

VII. RESULTS

As shown in Sec. V C above, the data are fully consistent with the possibility that all detected nuclear-recoil events are due to background neutron scatters and not WIMPs. For this

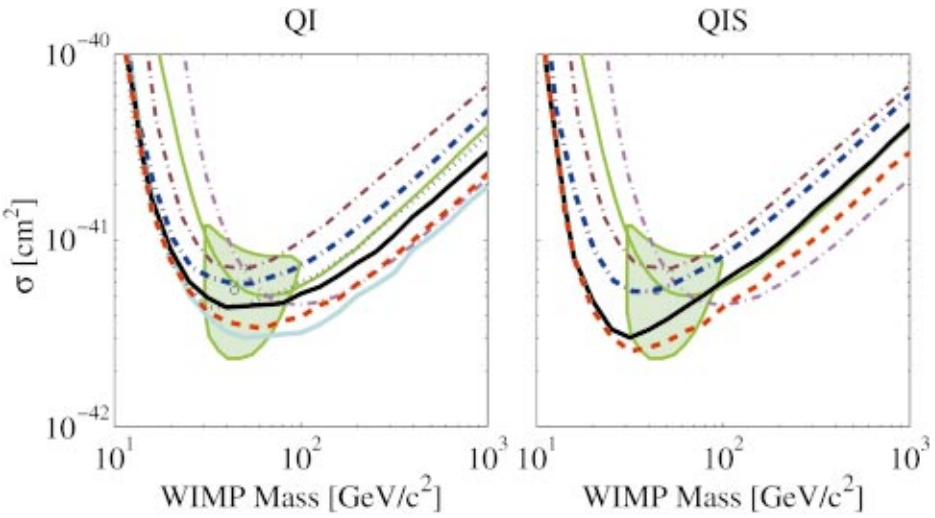

FIG. 46. (Color) Additional upper limits on the spin-independent WIMP-nucleon cross section σ, based on different treatments of the data, for both the QI (left) and QIS (right) data. The regions above the curves are excluded at 90% C.L. In each plot, CDMS limits including estimates of the neutron background, as described in Sec. VI, are shown as black solid curves. Limits calculated ignoring the 1998 Si data entirely (red dashed curves) would be better than these limits. Limits calculated ignoring all knowledge about the neutron background (thick dark blue dot-dashed curves) would still be the most sensitive upper limits of any experiment for WIMPs with masses between 10–45 GeV/c^2. The QI limit is worse than the CDMS QI limit previously reported [18] (light blue solid curve) primarily due to the more conservative treatment of the 1998 Si data. The QI limit is better than the expected sensitivity (black dotted curve) for high WIMP masses because more multiple-scatter neutrons were detected than expected. As in Fig. 45, the light green solid curve is the DAMA limit using pulse-shape analysis [65], the shaded region is the DAMA 3σ allowed region [66], the circle (x) indicates the DAMA best-fit point including (not including) the DAMA limit using pulse-shape analysis, the thin, dark (brown) dotted-dashed curve is the upper limit of the IGEX experiment [68], and the thin, light (maroon) dot-dashed curve is the upper limit of the EDELWEISS experiment [67].

reason, the data provide no lower limit on the WIMP-nucleon cross section. Figure 45 displays the upper limits on the WIMP-nucleon cross section calculated under the assumptions on the WIMP halo described in Sec. VI A; these values are the lower envelope of points excluded at the 90% confidence level for all values of the neutron background n.

Figure 45 also shows the expected sensitivity of the data set, i.e., the expected 90% C.L. exclusion limit given no expected WIMP signal, an expected background in the QIS Ge data set of 27 neutron events, and an expected background in Si of 7.2 electrons and 4.6 neutrons. To calculate these expected sensitivities, an ensemble of experiments are simulated, and the median resulting limit is taken (statistical fluctuations are large, so only 50% of the limits fall within $\pm 50\%$ of these median expected sensitivities). As indicated in the figure, the upper limit for the QIS data is slightly better than expected at low masses and slightly worse than expected at high masses; Fig. 46 shows that the upper limit of the QI data is slightly worse than expected at low masses and slightly better than expected at high masses. These results are consistent with statistical fluctuations.

For WIMP masses $M \gtrsim 100$ GeV/c^2, the expected WIMP energy spectrum matches that predicted for neutrons, so the estimate of the neutron background (based on the number of detected multiple-scatter neutrons and Si neutrons) has a dominant effect on the limits. Because the QIS data set represents a larger data set yet has no more multiple-scatter neutrons than the QI data set, its estimate of the neutron background is lower, and the QIS upper limits are slightly worse than the QI limits. For these WIMP masses, the upper limits correspond to expectations of ~ 23 (~ 13) WIMP interactions in the Ge single-scatter QIS (QI) data set, about the same as the actual number of observed events. As described above, these data are also consistent with no WIMP interactions.

For a low-mass WIMP, estimates of the neutron background have no effect. A low-mass WIMP would result in a sharply falling energy spectrum; only the events just above the energy threshold could be WIMPs. For this reason, at the lowest masses (10–15 GeV/c^2), the upper limits for the QI and QIS data sets are very similar. The smaller statistical uncertainty associated with the larger QIS data set makes its limits slightly better than the QI upper limits at low mass.

For intermediate WIMP masses, the energy spectrum of the Ge single-scatter events contributes to the estimate of the neutron background, with the number of high-energy events helping to set the neutron background. Because the QIS data set has a slightly harder energy spectrum than the QI data set, the QIS data set results in a larger neutron estimate and a lower upper limit on the WIMP signal for these moderate masses. Figure 47 shows the barely-excluded spectra for a sampling of WIMP masses.

These limits are lower than those of any other experiment for WIMPs with 10 GeV/$c^2 < M < 70$ GeV/c^2. According to the calculations presented in [11,70,71], these limits do not appear to exclude any parameter space consistent with the minimal supersymmetric standard model (MSSM) and allowed by accelerator constraints. Figure 48 compares these limits to the regions of parameter space consistent with various frameworks of the MSSM.

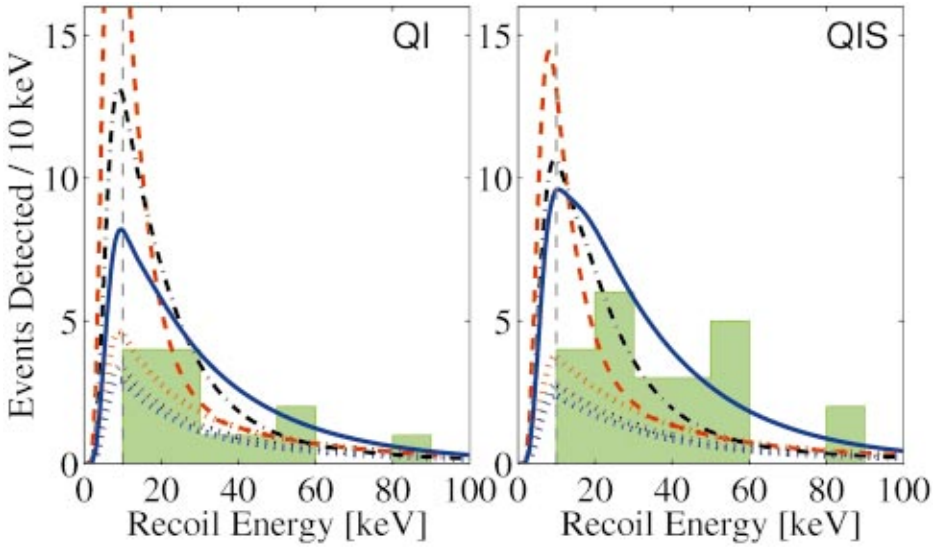

FIG. 47. (Color) Histograms of energies of WIMP-candidate events (green shaded) for both the QI (left) and QIS (right) data sets, compared with the spectra expected to be detected by CDMS for WIMPs excluded at exactly the 90% confidence level. Spectra for WIMPs with masses of 20 GeV/c^2 (red dashes), 40 GeV/c^2 (black dotted-dashes), and 125 GeV/c^2 (blue solid) are shown, including the expected contribution for the neutron background $\tilde{n}$ that maximizes the likelihood function for the given WIMP mass and WIMP-nucleon cross section (see Sec. VI). These most likely neutron backgrounds (shown separately as dotted curves) correspond to 1.0, 0.7, and 0.6 (1.1, 0.8, and 0.7) multiple-scatter QIS (QI) neutrons expected, given the WIMP masses of 33 GeV/c^2 (top curve), 67 GeV/c^2 (middle curve), and 216 GeV/c^2 (bottom curve). These low expected neutron backgrounds contribute to the unlikelihood of the WIMP models considered.

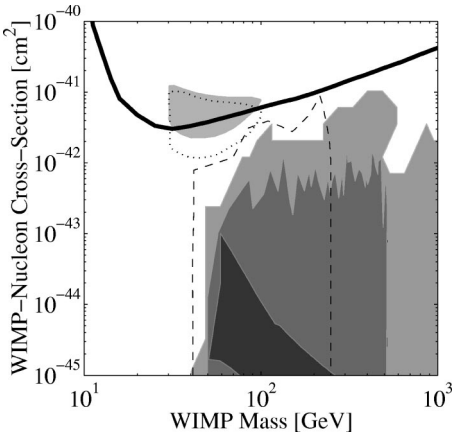

FIG. 48. CDMS upper limits on the spin-independent WIMP-nucleon cross section σ (dark curve), shown with the DAMA 3σ allowed regions including (dotted) and not including (light shaded region) the DAMA limit [66], as well as with regions of parameter space consistent with various frameworks of the MSSM and the standard WIMP interactions and galactic halo described above. The region outlined in dashes [11] and the lightest theoretical region [70] each shows the results from calculations under an effective scheme, with parameters defined at the electroweak scale. The medium-gray region [71] arises from constraining the parameter space to small values of $\tan\beta$, the ratio of vacuum expectation values of the two Higgs bosons. The darkest region represents the models allowed in a more constrained framework (called minimal supergravity or constrained MSSM), in which all soft scalar masses are unified at the unification scale [71].

As shown in Fig. 46, both the QIS and QI limits would be lower if the 1998 Si data were ignored. The conservative estimate of the amount of electron contamination in the nuclear-recoil band of the Si data reduces the estimate of the neutron background. This more conservative estimate of the Si contamination is the main reason that the QI limit is worse than that previously reported [18].

Figure 46 also shows the upper limits if all knowledge about the neutron background is ignored. The figure shows that even without any background estimation, CDMS limits are more sensitive for WIMPs with masses between 10–45 GeV/c^2 than those of any other experiment. Figure 49 shows the barely excluded spectra for a sampling of WIMP masses.

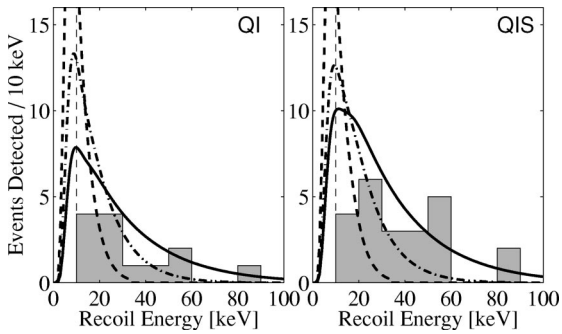

FIG. 49. Histograms of energies of WIMP-candidate events (shaded) for both the QI (left) and QIS (right) data sets, indicating the spectra expected to be detected by CDMS for WIMPs excluded at exactly the 90% confidence level if all knowledge about the background is ignored. Spectra for WIMPs with masses of 20 GeV/c^2 (dashes), 40 GeV/c^2 (dot-dashes), and 125 GeV/c^2 (solid) are shown.

Under the assumptions of standard WIMP interactions and halo, the QIS (QI) data with estimation of the neutron background exclude, at $>99.9\%$ ($>99\%$) C.L., the most likely value ($M=52$ GeV/$c^2, \sigma=7.2\times10^{-6}$ pb) for the spin-independent WIMP signal from the annual-modulation measurement reported by the DAMA Collaboration [66]. The QIS (QI) data exclude, at $>99\%$ ($>95\%$) C.L., the most likely value ($M=44$ GeV/$c^2, \sigma=5.4\times10^{-6}$ pb [66]) obtained by combining DAMA's annual-modulation measurement with their exclusion limit based on pulse-shape analysis [65]. The CDMS limits without any background estimation exclude, at 90% C.L. (at $>90\%$ C.L.), the most likely value for the WIMP signal from the DAMA annual-modulation measurement with (without) their exclusion limit based on pulse-shape analysis.

At 90% C.L., these data do not exclude the complete parameter space reported as allowed at 3σ by the annual-modulation measurement of the DAMA Collaboration. However, compatibility between the annual modulation signal of DAMA and the absence of a significant signal in CDMS (or in another experiment) is best determined by a goodness-of-fit test, not by comparing overlap regions of allowed parameter space. A likelihood-ratio test can determine the probability of obtaining a given combination of experimental results for the same parameters. The test involves calculating $\lambda \equiv \mathcal{L}_0/\mathcal{L}_1$, where $\mathcal{L}_0$ is the likelihood of the data assuming compatibility and $\mathcal{L}_1$ is the likelihood without assuming compatibility. If the data are compatible, $-2\ln\lambda$ should follow the χ^2 distribution with two degrees of freedom in the asymptotic limit of large statistics and away from physical boundaries. Under this approximation and the assumptions of standard WIMP interactions and halo, this test indicates the model-independent annual-modulation signal of DAMA (as shown in Fig. 2 of [66]) and CDMS data are incompatible at 99.99% C.L. Furthermore, even under the assumption that none of the CDMS events are due to neutrons, a likelihood-ratio test indicates the CDMS data and the DAMA signal are incompatible at 99.8% C.L. Simply put, a spin-independent WIMP-nucleon cross section that would give rise to the annual-modulation amplitude $A=0.022$ events $\mathrm{kg}^{-1}\,\mathrm{keV}^{-1}$ observed by DAMA averaged over 2–6 keV electron-equivalent energy should yield >3 events $\mathrm{kg}^{-1}\,\mathrm{day}^{-1}$ in Ge, incompatible with the 23 CDMS events in 15.8 kg d even if none of the events are due to neutrons. If the amplitude of the annual modulation observed by DAMA is a large statistical fluctuation, or if part of the modulation is due to something other than WIMPs, the CDMS and DAMA results may be compatible. Furthermore, if the distribution of WIMPs locally is much different than assumed (see, e.g. [72,73]), if WIMPs interact other than by spin-independent elastic scattering (see, e.g. [74–76]), or if WIMP interactions are otherwise different than assumed, the two results may be compatible.

ACKNOWLEDGMENTS

We thank Paul Luke of LBNL for his advice regarding surface-event rejection. We thank R. Abusaidi, J. Emes, D. Hale, G.W. Smith, J. Taylor, S. White, D.N. Seitz, J. Perales, M. Hennessy, M. Haldeman, and the rest of the engineering and technical staffs at our respective institutions for invaluable support. This work is supported by the Center for Particle Astrophysics, an NSF Science and Technology Center operated by the University of California, Berkeley, under Cooperative Agreement No. AST-91-20005, by the National Science Foundation under Grant No. PHY-9722414, by the Department of Energy under contracts DE-AC03-76SF00098, DE-FG03-90ER40569, DE-FG03-91ER40618, and by Fermilab, operated by the Universities Research Association, Inc., under Contract No. DE-AC02-76CH03000 with the Department of Energy.

[1] L. Bergstrom, Rep. Prog. Phys. **63**, 793 (2000).
[2] E.W. Kolb and M.S. Turner, *The Early Universe* (Addison-Wesley, Reading, MA, 1990).
[3] P.J.E. Peebles, *Principles of Physical Cosmology* (Princeton University Press, Princeton, NJ, 1993).
[4] P. de Bernardis *et al.*, Astrophys. J. **564**, 559 (2002).
[5] C. Pryke, N.W. Halverson, E.M. Leitch, J. Kovac, J.E. Carlstrom, W.L. Holzapfel, and M. Dragovan, Astrophys. J. **568**, 46 (2002).
[6] R. Stompor *et al.*, Astrophys. J. Lett. **561**, L7 (2001).
[7] D.E. Groom *et al.*, Eur. Phys. J. C **15**, 1 (2000), p. 143.
[8] G. Jungman, M. Kamionkowski, and K. Griest, Phys. Rep. **267**, 195 (1996).
[9] J. Ellis, T. Falk, K.A. Olive, and M. Schmitt, Phys. Lett. B **413**, 355 (1997).
[10] J. Edsjo and P. Gondolo, Phys. Rev. D **56**, 1879 (1997).
[11] A. Bottino, F. Donato, N. Fornengo, and S. Scopel, Phys. Rev. D **63**, 125003 (2001).
[12] J. Ellis, T. Falk, G. Gani, and K.A. Olive, Phys. Rev. D **62**, 075010 (2000).
[13] B.W. Lee and S. Weinberg, Phys. Rev. Lett. **39**, 165 (1977).
[14] P. Salucci and M. Persic, in ASP Conference Series No. 117: Dark and Visible Matter in Galaxies and Cosmological Implications 1997, edited by P. Salucci and M. Persic, pp. 1–27, astro-ph/9703027.
[15] M.W. Goodman and E. Witten, Phys. Rev. D **31**, 3059 (1985).
[16] J.R. Primack, D. Seckel, and B. Sadoulet, Annu. Rev. Nucl. Part. Sci. **38**, 751 (1988).
[17] J.D. Lewin and P.F. Smith, Astropart. Phys. **6**, 87 (1996).
[18] R. Abusaidi *et al.*, Phys. Rev. Lett. **84**, 5699 (2000).
[19] T. Shutt *et al.*, Phys. Rev. Lett. **69**, 3425 (1992).
[20] T. Shutt *et al.*, Phys. Rev. Lett. **69**, 3531 (1992).
[21] R.J. Gaitskell *et al.*, in *Proceedings of the Seventh International Workshop on Low Temperature Detectors*, edited by S. Cooper (Max Planck Institute of Physics, Munich, 1997), pp. 221–223.
[22] K.D. Irwin *et al.*, Rev. Sci. Instrum. **66**, 5322 (1995).
[23] R.M. Clarke *et al.*, in *Proceedings of the Seventh International Workshop on Low Temperature Detectors* [21], pp. 229–231; note that early designs of ZIPs are referred to as FLIPs in this and other references.

[24] R.M. Clarke *et al.*, in *Proceedings of the Second International Workshop on the Identification of Dark Matter*, edited by N.J.C. Spooner and V. Kudryavtsev (World Scientific, Singapore, 1999), pp. 353–358.
[25] R.M. Clarke, Ph.D. thesis, Stanford University, 1999, URL http://cosmology.berkeley.edu/preprints/cdms/Dissertations/rolandthesis.pdf
[26] R.M. Clarke *et al.*, Appl. Phys. Lett. **76**, 2958 (2000).
[27] B. Sadoulet *et al.*, Physica B **219**, 741 (1996).
[28] T. Shutt *et al.*, Nucl. Instrum. Methods Phys. Res. A **444**, 340 (2000).
[29] T. Shutt, Ph.D. thesis, University of California, Berkeley, 1993.
[30] B. Neganov and V. Trofimov, Otkrytiya, Izobret. **146**, 215 (1985).
[31] P.L. Luke, J. Appl. Phys. **64**, 6858 (1988).
[32] T. Shutt *et al.*, in *Low Temperature Detectors*, edited by F.S. Porter, D. McCammon, M. Galeazzi, and C.K. Stahle, AIP Conf. Proc. No. 605 (AIP, Melville, NY, 2002), pp. 513–516.
[33] A. Da Silva, Ph.D. thesis, The University of British Columbia, 1996.
[34] S.R. Golwala, Ph.D. thesis, University of California, Berkeley, 2000, URL http://cosmology.berkeley.edu/preprints/cdms/golwalathesis
[35] D.S. Akerib *et al.* (in preparation).
[36] N. Wang, Ph.D. thesis, University of California, Berkeley, 1991.
[37] A.H. Sonnenschein, Ph.D. thesis, University of California, Santa Barbara, 1999, URL http://cosmology.berkeley.edu/preprints/cdms/Dissertations/sonnenschein.ps
[38] D. Yvon *et al.*, Nucl. Instrum. Methods Phys. Res. A **368**, 778 (1996).
[39] S. Tamura, Phys. Rev. B **56**, 13 630 (1997).
[40] R.P. Welty and J.P. Martinis, IEEE Trans. Magn. **27**, 2924 (1991).
[41] R.P. Welty and J.P. Martinis, IEEE Trans. Appl. Supercond. **3**, 2605 (1993).
[42] J.D. Taylor *et al.*, Adv. Cryog. Eng. **41**, 1971 (1996).
[43] P.D. Barnes, Jr., Ph.D. thesis, University of California, Berkeley, 1996.
[44] D.S. Akerib *et al.*, Nucl. Instrum. Methods Phys. Res. A **400**, 181 (1997).
[45] A. Da Silva *et al.*, Nucl. Instrum. Methods Phys. Res. A **364**, 578 (1995).
[46] This lead was recovered from a sunken ship ballast near Nantes, France, and purchased from Lemer Pax, Protection Anti-X, 3 Rue de l'Europe, Zone Industrielle, F-44470 Carquefou, France.
[47] A. Da Silva *et al.*, Nucl. Instrum. Methods Phys. Res. A **354**, 553 (1995).
[48] J.O. Johnson and T.A. Gabriel, ORNL Technical Report TM-10340, 1988.
[49] A. Fassò *et al.*, in Proceedings of the Workshop on Simulating Accelerator Radiation Environments, Santa Fe, 1993.
[50] R. Brun and F. Carminati, CERN Program Library Long Writeup W5013, CERN, 1993.
[51] F.F. Khalchukov *et al.*, Nuovo Cimento Soc. Ital. Fis., C **6**, 3 (1983).
[52] National Instruments Corporation, 11500 N Mopac Expwy, Austin, TX 78759-3504.
[53] W.H. Press, S.A. Teukolsky, W.T. Vetterling, and B.P. Flannery, *Numerical Recipes in C: The Art of Scientific Computing* (Cambridge University Press, Cambridge, England, 1992).
[54] G.F. Knoll, *Radiation Detection and Measurement, Second Edition* (Wiley, New York, 1989).
[55] T.A. Perera, Ph.D. thesis, Case Western Reserve University, 2001, URL http://cosmology.berkeley.edu/preprints/cdms/Dissertations/tap_thesis.pdf
[56] W.T. Eadie, D. Drijard, F.E. James, M. Roos, and B. Sadoulet, *Statistical Methods in Experimental Physics* (North-Holland, Amsterdam, 1971).
[57] F.F. Khalchukov *et al.*, Nuovo Cimento Soc. Ital. Fis., C **18**, 5 (1995).
[58] P. Singer, in *Springer Tracts in Modern Physics*, edited by G. Höhler (Springer-Verlag, Berlin, 1974), Vol. 71, pp. 39–87.
[59] G.L. Cassiday, J.W. Keuffel, and J.A. Thompson, Phys. Rev. D **7**, 2022 (1973).
[60] W. Lohmann, R. Kopp, and R. Voss, CERN Technical Report 85-03, 1985.
[61] Y.-F. Wang *et al.*, Phys. Rev. D **64**, 013012 (2001).
[62] T. Saab *et al.*, in *Low Temperature Detectors* [32], pp. 497–500.
[63] G.J. Feldman and R. Cousins, Phys. Rev. D **57**, 3873 (1998).
[64] S. Yellin, Phys. Rev. D **66**, 032005 (2002).
[65] R. Bernabei *et al.*, Phys. Lett. B **389**, 757 (1996).
[66] R. Bernabei *et al.*, Phys. Lett. B **480**, 23 (2000).
[67] A. Benoit *et al.*, Phys. Lett. B **513**, 15 (2001).
[68] A. Morales *et al.*, Phys. Lett. B **532**, 8 (2002).
[69] R.J. Gaitskell and V. Mandic, interactive sensitivity plots for direct detection of WIMP dark matter, URL http://dmtools.berkeley.edu/limitplots/
[70] E.A. Baltz and P. Gondolo, Phys. Rev. Lett. **86**, 5004 (2001).
[71] J. Ellis, A. Ferstl, and K.A. Olive, Phys. Rev. D **63**, 065016 (2001).
[72] C.J. Copi and L.M. Krauss, astro-ph/0208010.
[73] P. Belli, R. Cerulli, N. Fornengo, and S. Scopel, Phys. Rev. D **66**, 043503 (2002).
[74] D. Smith and N. Weiner, Phys. Rev. D **64**, 043502 (2001).
[75] R. Bernabei *et al.*, Eur. Phys. J. C **23**, 61 (2002).
[76] R. Bernabei *et al.*, Phys. Lett. B **509**, 197 (2001).